Chair of Physical Metallurgy and Metallic Materials

Master's Thesis

Prediciting Phase Stability of TiAl-based High Entropy Alloys from First-Principles

Lukas Hatzenbichler, BSc

September 2022

Affidavit:
I declare in lieu of oath, that I wrote this thesis and performed the associated research myself, using only literature cited in this volume.

Date

Signature

Acknowledgements

I would like to thank my supervisor Priv.-Doz. Mgr. David Holec, PhD, or in more appropriate words my mentor and friend David, for his assistance in writing this thesis and even more important for all his support over the last years during my studies. In the position of Bachelor and Master student, I have not only experienced many interesting scientific discussions, but also hiking days and barbecues with him, which I all appreciated very much. He gave me the trust to involve me in his scientific work that provided me with the confidence to tackle every problem he faced me with. I grant him high credit for guiding me through the first years of my scientific career and supplying me with knowledge and experience, from which I will benefit the rest of my life.

Furthermore, it was a pleasure for me to be part of the computational materials science (CMS) research group. I am thankful for meeting many inspiring persons and for the companionable team-working environment.

Finally, the most important part is, to express my gratitude to my family, girlfriend and friends. From young age on my father Thomas represented my great idol and always supported me with all his experience from an academic as well as life perspective. My mother Manuela deserves great appreciation for always helping me out in all situations of everyday life with all her love, which took a heavy load off my shoulders. I am very thankful for having my sister Tanja, of which I am very proud of, with her husband Markus and my grandparents Brunhilde and Josef, who are always there for me. My aunt Andrea and uncle Harald with their children Theresa and Sebastian also represent an important part of my life. Without them it would not be possible to live this satisfied and carefree life.
Lastly, I would like to express my huge gratitude to my girlfriend. She encourages me in all circumstances and keeps me grounded. She is the human being, I want to enjoy every second of my life with. I am so happy to have her, without her every success would be worthless. I love you, Lea!

I owe this thesis and the accomplishment of my objectives to all of you!

Abbreviations

HEA	High Entropy Alloy
CCA	Complex Concentrated Alloy
DFT	Density Functional Theory
VASP	Vienna Ab Initio Simulation Package
BCC	Body-Centred Cubic
FCC	Face-Centred Cubic
HCP	Hexagonal Close-Packed
HF	Hartree-Fock
GGA	Generalized Gradient Approximation
LDA	Local Density Approximation
PBE	Perdew, Burke and Ernzerhof
PAW	Projector-Augmented Wave
PP	Pseudopotential
SQS	Special Quasi-random Structure
HPC	High-Performance Computing
VSC	Vienna Scientific Cluster
EMTO	Exact Muffin-Tin Orbital
CPA	Coherent Potential Approximation
SEM-BSE	Scanning Electron Microscope Back-Scattered Electron
XRD	X-Ray Diffraction
EDX	Energy Dispersive X-ray

Abstract

The demand for materials that withstand harsh conditions in high-performance applications has increased drastically in recent years. Due to the predicted outstanding properties of high entropy alloys (HEAs) at elevated temperatures, this class of materials has attracted scientific attention. Within this thesis, the phase stability of TiAl-based HEAs, namely TiAlNbV-Mo and TiAlNbV-Mn systems, is investigated by first-principles calculations using Density Functional Theory (DFT) as implemented in the VASP code. The aim is to find elements for a HEA that promote the formation of a single-phase solid solution alloy and do not have the tendency to decompose into intermetallic phases. The information on the phase stability is provided by the evaluation of mixing energies. First of all, the stability of the HEAs and their possible decomposition products are evaluated at 0 K. Furthermore, the stabilizing effect of entropy is included by the contribution of the configurational entropy followed by the vibrational entropy estimated within the harmonic Debye model. Results obtained by the Exact Muffin-Tin Orbitals (EMTO) method are also presented for comparison. The predicted phase stabilities are discussed in light of existing experimental literature results showing the evolution of microstructure before and after heat treatments. Overall, TiAlNbV-Mo has been identified as a kinetically stabilized HEA, whereas TiAlNbV-Mn decomposes into body-centered cubic and hexagonal Laves phases.

Kurzfassung

Der Bedarf an Materialien, die die rauen Bedingungen bei Hochleistungsanwendungen standhalten müssen, ist in den letzten Jahren drastisch gestiegen. Aufgrund der vorausgesagten herausragenden Eigenschaften von Hochentropielegierungen (HEAs) bei hohen Temperaturen, hat diese Materialklasse die Aufmerksamkeit der Wissenschaft auf sich gezogen. Im Rahmen dieser Arbeit wird die Phasenstabilität von TiAl basierten HEAs, nämlich TiAlNbV-Mo und TiAlNbV-Mn, mittels ab initio Berechnungen unter Verwendung der Dichtefunktionaltheorie, implementiert in VASP, untersucht. Das Ziel ist es Elemente für eine HEA zu finden, die die Bildung von einphasigen Mischkristallen begünstigen und keine Neigung besitzen sich in der Form von intermetallische Phasen zu entmischen. Die Information für die Phasenstabilität von HEAs liefert die Auswertung von Mischungsenergien. Als erstes wird die Stabilität der HEAs und deren möglichen Entmischungsprodukte bei 0 K betrachet. In weiterer Folge wird zusätzlich der stabilisierende Effekt der Entropie miteinbezogen, zuerst durch den Anteil der strukturmäßigen Entropie, gefolgt von der Schwingungsentropie, die durch das Debye Modell abgeschätzt wird. Zum Zwecke der Vergleichbarkeit werden auch Ergebnisse der Exact Muffin-Tin Orbitals (EMTO) Methode dargelegt. Die vorhergesagten Phasenstabilitäten werden im Licht von bereits in der Literatur existierenden Ergebnissen, welche die Entwicklung der Mikrostruktur vor und nach Wärmebehandlung zeigen, diskutiert. Im Großen und Ganzen konnte TiAlNbV-Mo als kinetisch stabilisierte HEA identifiziert werden, wohingegen sich TiAlNbV-Mn in kubisch raumzentrierte und in hexagonale Laves Phasen entmischt.

Contents

Chapter 1

Introduction

The phenomenon that High Entropy Alloys (HEAs) attracted huge interest in the last years is based on their expected ability to withstand high temperatures and exhibit outstanding properties, such as high hardness, fracture toughness, fatigue-, wear-, oxidation- and corrosion resistance [1]. HEAs consist of at least five different, often metallic, elements contained in the equiatomic composition [2, 3]. Due to the combination of various elements, one would expect a high probability that intermetallic phases will be formed. However, the dominant feature of this material group, namely the high entropy or rather the high configurational entropy contribution, works against the decomposition of the alloy. Scientists aim for these alloys due to their high potential for high-performance applications, such as in the aviation or automotive industry, although it still turns out to be a challenging task to discover stable single-phase HEAs. Nevertheless, the investigation of HEAs (quinaries) and their equiatomic decomposition products (unaries, binaries, ternaries or quaternaries) will be the focus of this thesis.

The first stable single-phase HEA, the well-known Cantor alloy CrMnFeCoNi, was discovered in the early 1980s [4]. Since this time, only a little research has been done on these special alloys until the last decade. One reason for this long period without any success in this field was, that the experimental investigation of such a huge amount of possible elemental combinations is very effortful. This can be overcome by employing modelling techniques such as Density Functional Theory (DFT) [5]. DFT is, however, extremely demanding on resources. Recent advances in hardware and available computational power have led to a renewed surge of interest. DFT, as implemented in the Vienna Ab initio Simulation Package (VASP) [6, 7], turns out to be the perfect approach to deal with the high variety of HEAs and to detect candidates for stable alloys.

The ambition to find a lightweight HEA is fulfilled by going in the direction of TiAl-based alloys. The presence of Al, however, often promotes the formation of intermetallic phases [8], especially in combination with Ti [9]. Nevertheless, investigations from literature predict that

TiAlNbV solidifies in a single-phase body-centred cubic (BCC) microstructure [10], though the thermodynamic stability has been proven to be insufficient [11]. This stability should be increased by adding Mo or Mn [12], both known BCC phase stabilizers [13]. In the case of TiAlNbV-Mo, a stable ordered B2 microstructure has been already detected [14]. Hence, the phase stability of TiAlNbV-Mo is promising and will be further investigated. Regarding the TiAlNbV-Mn HEA, it is only known that the intermixing of TiAl and Mn leads to the precipitation of the hexagonal close-packed (HCP) C14 Laves phase [15]. However, in literature no further data about the phase stability of TiAlNbV-Mn has been found and hence will be provided in this thesis.

Chapter 2

Theoretical Background

2.1 General Definition of High Entropy Alloys

HEAs are named after their most important characteristic, their high entropy. More precisely expressed, it is the configurational entropy S_{conf} that makes these alloys special. In terms of numbers, a HEA is supposed to have a configurational entropy higher than $1.61R$, R is the ideal gas constant ($= 8.314$ J/(mol $\cdot$ K) [16]). This value exactly represents the configurational entropy of an equimolar five-element solid solution. Hence, a HEA is typically consisting of five or more elements with equiatomic—or at least near-equiatomic—composition [2, 3]. The consequence of the high configurational entropy is a stabilization effect of single-phase solid solutions above 0 K and especially at high temperatures. Other contributions concerning the entropy—vibrational, electronic and magnetic—exist, but it is assumed that they have negligible impact. Another requirement for a HEA is that its elements must be fully miscible so that a single-phase solid solution can be obtained [17]. Therefore, a careful selection of elements has to be made.

Over time it turned out that researchers felt limited in their scientific freedom by this strict definition of HEAs. They classified the alloys with respect to their entropy, namely in medium entropy alloys ($1R < S_{conf} < 1.5R$) and low entropy alloys ($S_{conf} < 1R$) [18]. Moreover, the term complex concentrated alloys (CCAs) evolved, which extends the field of HEAs by also considering multiphase alloys. CCAs are not restricted to equimolar compositions and may contain less than five elements [19, 20]. This is why the expression HEA is lately often replaced by CCA. This work aims to investigate and find a five-component single-phase solid solution alloy which fulfils the definition of a HEA. Hence, for the sake of simplicity, the term HEA represents five-component (quinary) alloys within the scope of this thesis. The attention of researchers got attracted, when they noticed that HEAs could have a unique combination of attractive properties based on their fundamental effects at the atomic scale.

2.2 Core Effects and Outstanding Properties

The demand to develop new materials with outstanding properties for high-performance applications is steadily increasing. The fact that HEAs have been lately highly recognized in this field is closely linked to four core effects. These effects should not only lead to high hardness, fracture toughness, fatigue-, wear-, oxidation- and corrosion resistance at ambient temperature, but they should be retained in heated environments as well [1, 21].

2.2.1 High Entropy Effect

High entropy plays the most important role in the concept of HEAs. Mathematically, Gibb's law demonstrates how Gibb's free energy, ΔG_{mix}, influences the stability of a phase considering the entropy as well as enthalpy, ΔS_{mix} and ΔH_{mix}, respectively, at a certain temperature T. To highlight the dominance of the configurational entropy, ΔS_{conf}, in HEAs, we insert this characteristic variable directly into Gibb's law instead of the total mixing entropy. Gibb's law then reads as:

$$\Delta G_{mix} = \Delta H_{mix} - T\Delta S_{conf}. \tag{2.1}$$

A decrease of Gibb's free energy corresponds to a higher stability of a certain single-phase solid solution. From here, it can be clearly seen that increasing entropy leads to stabilization and suppresses the precipitation of ordered intermetallic phases. Additionally, the elevation of temperature T greatly impacts the free energy minimization of a phase [2, 3, 22]. This is also stated in a work of Luan *et al.* [23], where they point out the increasing percentage of single-phase alloys with increasing temperature. However, it should be kept in mind that the overall possibility of finding single-phase alloys decreases with a higher variety of elements. Nevertheless, due to their configurational entropy, the chances of forming single-phase solid solutions are more pronounced in HEAs, especially at higher temperatures. The positive consequence of preventing the formation of brittle intermetallic phases is that it guarantees improved mechanical properties at elevated as well as ambient temperatures.

2.2.2 Sluggish Diffusion Effect

Researchers claim in several works that the diffusion of atoms and phase transformation kinetics are much slower in HEAs than in conventional alloys [24, 25]. This is because of the variety of chemical bonds, the complex atomic configurations and the high number of different activation energies for diffusion [2]. Nevertheless, the existence of this effect has been put under scrutiny recently, and further investigations have been done. Dabrowa *et al.* [26] suggested that this effect does not originate from the high disorder in HEAs, but from specific elemental compositions. For instance, they observed sluggish diffusion only in alloys with high Mn contents independent of the number of elements [26]. It is only confirmed that

the element with the lowest diffusion coefficient is the limiting factor for the velocity of the net diffusion process [27]. The exact mechanisms behind this effect are therefore still under debate and have to be investigated further.

2.2.3 Severe Lattice Distortion Effect

In HEAs, several different species of atoms occupy one lattice. The variety of atomic radii inevitably leads to a lattice distortion, which can be estimated from the atomic size difference δ of the components that assemble the alloy [28]:

$$\delta = \sqrt{\sum_{i=1}^{N} c_i(1 - r_i/\bar{r})}. \tag{2.2}$$

Here, N is the number of elements, c_i and r_i are concentration and radius of the i^{th} element, and $\bar{r}$ denotes the average atomic radius of all components. The higher δ, the more pronounced the distortion of the lattice, which hinders the dislocation movement and acts as the main contribution to solid solution strengthening. Consequently, this effect influences mechanical as well as electrical and thermal properties. High hardness, strength and softening resistance at high temperatures of HEAs can be partly ascribed to the distortion of the lattice. The thermal and electrical conductivities decrease stronger the more distinct this effect is, which is related to a higher degree of electron and phonon scattering in the lattice [2, 29]. However, the distortion depends not only on the size difference of atoms but also on the number of elements in the alloy. Other unknown circumstances definitely play a role as well. Determining the degree to which the lattice distortion affects the properties of HEAs turns out not to be a simple task because other properties/features in HEAs may have a similar impact [28].

2.2.4 Cocktail Effect

The addition of an element to an alloy changes its properties. Intuitively we can assume that by mixing an element with a predominant property to an alloy, exactly this property will be intensified. For instance, assumptions would be that the addition of refractory elements improves high-temperature properties or light elements decrease the density. The cocktail effect describes the fact that unusual combinations of elements, such as those present in HEAs, can behave in the exact opposite way and lead to unique properties [2]. The reason for such behaviour traces back to the interactions between the different atoms. Alloying of Al leads to a significant hardness increase, although Al is relatively soft compared to other metals. However, it has to be considered that Al builds very strong bonds with other elements and promotes the formation of hard phases with body-centred cubic (BCC) structure. Additionally, the solid solution strengthening process is of major relevance [2, 8].

Therefore, the unexpected behaviour due to the cocktail effect is another incidence, which makes the task to discover and select reasonable elements for HEAs quite complicated.

2.3 Selection of Elements for HEAs and the Role of TiAl

The detection of random combinations of elements that form single-phase solid solutions is a relatively rare case. A first step to enhance the chances to reach this goal is the implementation of the so-called Hume-Rothery rules [30] during the elemental selection. These rules contain prerequisites regarding the atomic configuration of the different elements in an alloy:

1) Atomic radii of the components should not differ more than 15%.

2) The difference in the electronegativities should be as small as possible.

3) The number of the valence electrons should be similar.

However, this results in just a small reduction of the huge number of possible elemental combinations for HEAs. After the selection of elements via these rules, further filtering by, e.g. the calculation and comparison of mixing enthalpies of the alloy itself and its decomposition products can be done [31, 32]. Such techniques will be applied in the *Results and Discussion* (Chap. 4) part of this thesis.

The selection of elements in this work is based on a paper from Stepanov [10], where they studied the mechanical properties of an equiatomic single-phase solid-solution TiAlNbV alloy. This study not only predicted a very low density of the alloy but also a high specific yield strength at elevated temperatures. Unfortunately, the improvement of strength at ≈ 800 °C is attributed to a decomposition process into intermetallic phases leading to unfavourable embrittlement at ambient temperatures [11]. As TiAlNbV still is a very promising lightweight alloy for high-temperature applications, the idea is to stabilize it via implementing the fifth element. Attempts to reach this goal failed with TiAlNbV-Cr and TiAlNbV-Zr [33, 34]. For an application-relevant success, it is desirable that the HEA crystallizes in a stable single BCC phase so that the precipitation of intermetallic phases is suppressed. The expectation is to promote this by adding transition metals, which crystallize in the BCC structure itself. Following this idea and the Hume-Rothery rules, we decided on Mo and Mn as an additional element within the scope of this thesis. In Tab. 2.1 it can be seen that the atomic radius of Mo fits perfectly to the other elements and also the radius of Mn is in the range of 15 % compared to the average radius of all contained elements. Both elements, Mo and Mn, prefer the BCC structure in their ground state and their valency, indicated with the electronic configuration, is similar to the other elements. In comparison, the electronegativity

is relatively high, but still should be in an acceptable range. Hence, the phase stability of TiAlNbV-Mo, TiAlNbV-Mn, and their possible decomposition products will be analyzed within this work.

Table 2.1: Important values for the elemental selection according to Hume-Rothery rules obtained from Merck Periodic Table of Elements [35].

Element	Atomic Radius [pm]	Crystal Structure	Electronegativity	Electronic Configuration
Ti	145	hcp	1.54	[Ar] 3d2/4s2
Al	143	fcc	1.61	[Ne] 3s2/3p1
Nb	146	bcc	1.60	[Kr] 4d4/5s1
V	134	bcc	1.63	[Ar] 3d3/4s2
Mo	139	bcc	2.16	[Kr] 4d5/5s1
Mn	127	bcc	1.55	[Ar] 3d5/4s2

2.4 Thermodynamic Fundamentals of Decomposition

A simple mixing reaction of two components A and B consolidating into an alloy AB can be expressed by the following equation:

$$A + B \leftrightarrow AB. \tag{2.3}$$

Whether the chemical reaction is more prone to go towards right or left direction is determined by Gibb's free energy of mixing ΔG_{mix}. On the one hand, a negative value of ΔG_{mix} predicts a stable mixture AB, a positive one leads to the decomposition into its components A and B [36]. For the first-principles study of phase stability of HEAs an extension of the Gibb's law (see Eq. (2.1)) has been done. In general, the mixing enthalpy ΔH_{mix} can be formulated via the total ground state energies of the alloy, $E(AB)$, and of its components, $E(A)$ and $E(B)$, multiplied by their corresponding mole fractions x_A and x_B:

$$\Delta H_{mix} = E(AB) - [x_A E(A) + x_B E(B)]. \tag{2.4}$$

At 0 K ΔH_{mix} is equal to ΔG_{mix} and quantifies the stability with respect to isostructural decomposition of the unaries. It exists also a similar approach, namely the formation energy, which defines the stability with respect to the unary elements in their equilibrium structure. Both quantities can provide a first evidence about the stability of alloys, e.g. negative values indicate a stable alloy and vice versa. At 0 K both, ΔH_{mix} and the formation energy, lead to exactly the same results with respect to unaries. However, in this thesis we will stick to the ΔH_{mix} term.

For the further study of the phase stability and the decomposition behaviour of HEAs, AB will refer to the HEA itself and the components A and B to its corresponding decomposition

products. Hence, x_A and x_B denote the ratio of the phase components or the decomposed products in the HEA. We note that there may be more than 2 decomposition products; for the sake of simplicity, we introduce the formalism here using only two components. Moreover, the entropy term is reduced to the configuration entropy S_{conf}, which can be calculated simply by knowing the mole fractions ξ_i of the components i forming an alloy X, and the Boltzmann constant k_B [23]:

$$S_{conf}(X) = -k_B \sum_i \xi_i \ln \xi_i. \tag{2.5}$$

Finally, ΔG_{mix} for a HEA AB and a certain decomposition route into products A and B can be calculated with the following equation:

$$\begin{aligned} \Delta G_{mix} =& E(AB) - [x_A E(A) + x_B E(B)] - \\ & - T[S_{conf}(AB) - [x_A S_{conf}(A) + x_B S_{conf}(B)]. \end{aligned} \tag{2.6}$$

In this formulation, all material quantities are determined by the first-principles calculations; mole fractions x_i and temperature T are external parameters. This turns out very useful, because the temperature T can take any arbitrary value, although no temperature effects, such as phonons, have been considered until now. As a consequence, also the phase stability at elevated temperatures can be predicted in a very practical manner.

Keeping in mind the previous assumptions, the following conclusion can be drawn from ΔG_{mix}:

$$\Delta G_{mix} \begin{cases} < 0: & \text{HEA is stable,} \\ > 0: & \text{HEA decomposes into its decomposition products.} \end{cases}$$

2.5 Stabilization of HEAs via Volume Mismatch

Another important factor during decomposition is the volume mismatch between the HEA and its potential decomposed phases. Decomposition products often form compounds with higher or lower specific volumes than the actual HEA [36, 37]. However, when the decomposition starts, these products still have to fit in the volume of the parent HEA phase as no relaxation is allowed due to the surrounding matrix (still the parent HEA phase). This effect emerges through the elastic strain energy. A measure of the strain energy can be stated by the actual difference of the volume of the HEA and its corresponding decomposition products, ΔV. The HEA volume $V(AB)$ and the average volume of the decomposition products $V_{mean}(A, B)$ gives an estimation of the extent of elastic strain energy [38]:

$$\Delta V = \frac{V(AB) - V_{mean}(A, B)}{V(AB)}. \tag{2.7}$$

The consequence of a high volume difference, $|\Delta V|$, is a stabilization effect on the HEA. ΔV decreases the mixing enthalpy of the system and the activation energy for decomposition is raised by the additional elastic strain energy [36]. Hence, elements that tend to form high-volume structures with other components would need more energy to precipitate, i.e. higher temperatures. This has a positive effect on the phase stability of HEAs and their single-phase solid-solution phase is more likely to be maintained.

2.6 Implementation of Debye Model

Thermodynamic quantities of a material can be characterized by lattice vibrations, namely phonons. These quantized quasiparticles describe the thermal excitation of atoms in a periodic crystal [39]. Energetically, phonons are responsible for the main temperature-dependent contributions to the free energy as well as to the entropy of a system.

For the sake of simplicity, let us consider vibrating crystals as a collection of harmonic oscillators that oscillate around their equilibrium positions with a frequency ω. Moreover, in the Debye model the crystal is assumed as an elastic continuum wherein sound waves propagate with constant velocity. This sound velocity v_s acts as a proportionality factor between the frequency of the vibrations and the wave number k:

$$\omega(k) = v_s k. \tag{2.8}$$

In general, such a dispersion relation $\omega(k)$ describes how a wave is behaving in a medium. The sound waves are elastic waves that penetrate through a material. Therefore, it is possible to construct a connection from the velocity of sound—and therefore lattice vibrations—to the material's elastic properties. As an example, such important correlation between ω, v_s and the elastic constant C_{11} is demonstrated for a cubic material and an elastic wave propagating in the $\langle 100 \rangle$ direction [40]:

$$v_s = \frac{\omega}{k} = \sqrt{\frac{C_{11}}{\rho}}. \tag{2.9}$$

The density ρ acts here as an intensive physical quantity of a certain material. The higher ρ, the lower will be ω and therefore v_s [39]. Based on these ideas it becomes immediate that the elastic response of a material is closely related to the thermally excited vibrations in its lattice.

In the Debye model the relation is established through the bulk modulus. This material quantity can be derived from its corresponding elastic matrix C_{ij} that is obtained, e.g., from the stress-strain method and first-principles calculations (see Sec. 2.7). The bulk modulus is assumed as static in this model, which refers to very slow deformations. Moreover, the model

approximates that the solid acts as a fluid and therefore no shear deformations ($C_{44} = 0$) take place. Therefore, only longitudinal lattice vibrations are considered and denotes the loading direction of C_{11}. With this assumption an average of the sound velocity can be obtained:

$$\bar{v_s} \approx \sqrt{\frac{C_{11}}{\rho}} \approx \sqrt{\frac{B_{static}}{\rho}}. \tag{2.10}$$

To retain the accuracy of the method, a function to describe the ratio between transverse and longitudinal deformation is implemented. This function $f(\nu)$ depends solely on the Poisson's ratio ν and modifies the Eq. (2.10) to [40]:

$$\bar{v_s} \approx \sqrt{\frac{B_{static}}{\rho}} f(\nu). \tag{2.11}$$

For the calculation of the vibrational free energy within the Debye model a first-principles study from Chakraborty *et al.* [41] was chosen as a methodological reference. In that study, they investigated the martensitic transformation temperature of TiTa following this model. Firstly, the function of the Poisson's ratio $f(\nu)$ is generally calculated as:

$$f(\nu) = \left\{ 3 \left[2 \left(\frac{2}{3} \frac{1+\nu}{1-\nu} \right)^{3/2} + \left(\frac{1}{3} \frac{1+\nu}{1-\nu} \right)^{3/2} \right]^{-1} \right\}^{1/3}. \tag{2.12}$$

The Poisson's ratio itself can be obtained from the elastic constants, or rather from the bulk modulus together with the shear modulus obtained by the stress-strain method (see Eq. (2.21)). As a next step, the Debye temperature θ_D is calculated for an isotropic solid considering the approximations mentioned (Eq. (2.10) and Eq. (2.11)):

$$\theta_D = \frac{\hbar}{k_B} [6\pi^2 V^{1/2} n]^{1/3} f(\nu) \sqrt{\frac{B_{static}}{M}}. \tag{2.13}$$

θ_D defines the temperature, where all vibrational states have been occupied. Additionally to ν and B_{static}, θ_D is dependent on the volume V, the number of atoms per formula unit, n, and the molecular mass, M, per formula unit. The two constants k_B and $\hbar$ denote the Boltzmann and the reduced Planck constants. Moreover, a Debye function $D(\theta_D/T)$ needs to be defined, which is given by:

$$D(\theta_D/T) = 3 \left(\frac{T}{\theta_D} \right)^3 \int_0^{\theta_D/T} \frac{x^3}{e^x - 1} dx. \tag{2.14}$$

Finally, the vibrational free energy, F_{vib}, is calculated as follows:

$$F_{vib}(\theta_D(V), T) = n k_B T \left[\frac{9}{8} \frac{\theta_D(V)}{T} + 3 \ln \left(1 - e^{-\theta_D(V)/T} \right) - D(\theta_D(V)/T) \right]. \tag{2.15}$$

To obtain F_{vib}, this procedure can be used in two ways: The first way defines the purely harmonic approximation, which has the disadvantage that important thermal quantities, such as the thermal expansion, cannot be obtained. This is because it depends on the asymmetry of the vibrational potential, which is genuinely neglected in the harmonic approximation. Secondly, also a quasiharmonic approach exists to overcome this problem, which considers harmonic approximations at several volumes in addition to the equilibrium 0 K volume [40].

For the sake of simplicity, this thesis is restricted to the simple harmonic approximation applied to the equilibrium volumes and bulk moduli at $T = 0$ K directly obtained from the first-principles calculations. Nevertheless, it should serve as a first attempt to include thermal effects beyond configurational entropy. Including this energy term in Eq. (2.6), the Gibb's free energy of mixing reads:

$$\begin{aligned}\Delta G_{mix} =& E(AB) - [x_A E(A) + x_B E(B)] - \\ &- T[S_{conf}(AB) - [x_A S_{conf}(A) + x_B S_{conf}(B)] + \\ &+ \underbrace{F_{vib}(AB) - [x_A F_{vib}(A) + x_B F_{vib}(B)]}_{-T\Delta S_{vib}}.\end{aligned} \tag{2.16}$$

The energy of the lattice vibrations in principle contains the contribution to the vibrational entropy of the system, which is enclosed in the $T\Delta S_{vib}$ term. The goal is to find out, if the vibrational entropy influences the free energy of HEAs in such an extent that further stabilization effects can be expected.

2.7 Calculation of Bulk Modulus: Stress-Strain Method

After obtaining the ground state parameters from first-principles calculations, the stress-strain method [42] is utilized to get the elastic tensor of the fully relaxed structures. An advantage of running first-principles calculations using the VASP code (see Sec. 3.4.1) is that stress tensors are easily obtained as output of the investigated structures. Consequently, if a set of linearly independent strains $\underline{\underline{\varepsilon}}_i$ will be applied manually, Hooke's law can be solved in the following way:

$$\underline{\underline{\sigma}}\ \underline{\underline{\varepsilon}}^{-1} = \underline{\underline{C}}. \tag{2.17}$$

Here, $\underline{\underline{C}} = (C_{ij})$ represents the matrix of elastic stiffness constants and $\underline{\underline{\sigma}} = (\underline{\sigma}_i)$ the set of stress tensor in the Voigt's notation [42, 43]. It is important that the strains do not exceed the elastic regime, therefore test calculations with different magnitudes of $\varepsilon = |\underline{\varepsilon}|$ have been executed (Appendix A). Based on these we concluded that strains up to ≈ 0.03 are acceptable for nearly all systems. For this study a value of $\varepsilon = 0.021$ is used to guarantee correct results.

After the C_{ij} matrix is directly calculated from the Hooke's law (Eq. (2.17)), it has to be symmetrized and projected to the corresponding crystal structure. The projection of C_{ij} works by averaging some components and setting other ones to zero. In the case of a cubic system, three elastic constants, C_{11}, C_{12}, C_{44} remain and they are calculated as [44]:

$$\overline{C_{11}} = \frac{1}{3}(C_{11} + C_{22} + C_{33}) \tag{2.18}$$

$$\overline{C_{12}} = \frac{1}{3}(C_{12} + C_{13} + C_{23}) \tag{2.19}$$

$$\overline{C_{44}} = \frac{1}{3}(C_{44} + C_{55} + C_{66}) \tag{2.20}$$

The Voigt-Reuss-Hill approximation for polycrystalline materials is utilized to calculate the Young's modulus, E, shear modulus, G, and bulk modulus, B, from the gathered elastic constants [45–47]. Moreover, G and B can be used to obtain the Poisson's ratio ν [41]:

$$\nu = \frac{3B - 2G}{2(3B + G)}. \tag{2.21}$$

The stress-strain method is a highly efficient method to calculate elastic properties of different materials in combination with first-principles calculations.

Chapter 3

Methodology

This chapter gives an overview of developments starting from the formulation of the Schrödinger equation and leading to Density Functional Theory (DFT). The approximations of Hartree and Fock as well as the unrivalled approach of DFT represent the basis for an accurate solution of the Schrödinger equation and, therefore enable computational materials science at the electronic structure level.

3.1 Schrödinger Equation

It dates back to 1924, when de Broglie published a paper about the discovery of the wave-particle duality of electrons [48]. After this striking success, scientists tried to express the electron's wave nature in terms of energy through a mathematical form. Only two years later, the Austrian physicist, Erwin Schrödinger, established the famous wave equation

$$\hat{H}\Psi(r_i, r_l) = E\Psi(r_i, r_l), \tag{3.1}$$

which represents a partial differential equation leading to an eigenvalue problem. The equation in general depends on the positions of the electrons, r_i, and nuclei, r_l [49]. The Hamiltonian operator, $\hat{H}$, contains all the corresponding energies of the particles, namely the kinetic energies as well as the potential Coulomb energies between all electron-nucleus, nucleus-nucleus and electron-electron pairs. $\hat{H}$ operates on the wave function Ψ, which gives back the total energy of the system E as output, the eigenvalue of the equation. Here, the time-independent Schrödinger equation is demonstrated, although there also exists a time-dependent version, which is much more complicated. In order to describe the quantum mechanical phenomena in a material, e.g. as it is done by first-principles calculations, the Schrödinger equation has to be solved. However, approximations have to be done to obtain proper solutions, which will be discussed in the upcoming sections. First-principles or rather *ab initio* means that a problem is solved straight from physical fundamentals. Therefore, the

equation can be seen as the foundation of computational materials science as all ground-state properties can be, in principle, determined without any experimental fitting [50, 51].

3.1.1 General Simplifications

The first-principles calculations focus on the ground state energies of electrons while the external potential of the system can be assumed as constant in time. Hence, the time-dependence of the wave function vanishes, which simplifies the equation to a time-independent problem. Moreover, gravity can be excluded due to the very small mass of electrons. Another well-known behaviour of electrons is their spin, which is in most cases disregarded but can be included if necessary [50]. These assumptions simplify the problem, but the consideration of all interactions between the particles still leads to highly complex conditions. One advanced approach to handle this problem is the Hartree-Fock method.

3.2 Hartree-Fock Method

The aim of the Hartree-Fock (HF) method [52] is to describe the Coulomb interactions between the electrons via quantum mechanical approaches. It is the first reasonably accurate approach to solve the Schrödinger equation. The first step is to separate the motion of nuclei and electrons. The justification for such treatment is known as the Born-Oppenheimer approximation [53]. Due to the much higher mass of the nuclei, it is claimed that the electrons can follow their motion immediately. Consequently, it is valid to write the total wave function as a product of two independent wave functions:

$$\Psi(r_i, r_l) = \Psi_{electronic}(r_i) \times \Psi_{nuclear}(r_l). \tag{3.2}$$

This assumption leads to separating out behaviour of only electrons, and hence formulating the Schrödinger equation only for the electronic system:

$$\hat{H}_{electronic}\Psi_{electronic}(r_i) = E\Psi_{electronic}(r_i). \tag{3.3}$$

In contrast to the full Hamiltonian $\hat{H}$, the electronic Hamiltonian, $\hat{H}_{electronic}$, does not include kinetic energies of the nuclei, $\hat{T}_n$, and the nucleus-nucleus Coulomb interactions, $\hat{U}_{n-n}$. This emerges from the assumption that the nuclei behave as they were static and thus the interaction between them is constant. In the below, we focus only on the electronic system and hence will omit the *electronic* subscript for the sake of simplicity. The electronic Hamiltonian operator reads

$$\hat{H} = \underbrace{-\frac{\hbar^2}{2m_{el}}\sum_i^N \nabla_i^2}_{\hat{T}_e} \underbrace{-\frac{1}{4\pi\epsilon_0}\sum_i^N\sum_l^M \frac{Z_l e}{|r_i - r_l|}}_{\hat{U}_{n-e}} + \underbrace{\frac{1}{8\pi\epsilon_0}\sum_{i\neq j}^N \frac{e^2}{|r_i - r_j|}}_{\hat{U}_{e-e}}, \tag{3.4}$$

where the kinetic energy, $\hat{T}_e$ involves the electron's mass, m_{el}, as well as the Laplace operator ∇_i^2 applied to the i^{th} electron. The attractive Coulomb potential between N electrons and M nuclei is described by the $\hat{U}_{n-e}$ term. There, ϵ_0 denotes the vacuum permittivity, Z_l the charge of the nucleus l and e the elemental charge. Lastly, $\hat{U}_{e-e}$ is the mathematical representation of the repulsive Coulomb potential between electrons.

Although this seems like a promising approximation, the solution of this equation for more than two electrons is still not manageable. This is related to the fact that the partial differential equation depends on $3N$ coordinates of N interacting electrons, which is defined as the many-electron problem:

$$\hat{H}\Psi(r_1, r_2, \ldots, r_N) = E\Psi(r_1, r_2, \ldots, r_N). \tag{3.5}$$

Hartree tried to overcome this by treating every electron individually. Hence, the many-electron wave function is split up via a product ansatz:

$$\Psi(r_1, r_2, \ldots, r_N) = \phi_1(r_1)\phi_2(r_2)\ldots\phi_N(r_N). \tag{3.6}$$

The interaction between the individual electrons is averaged and expressed by the so-called Hartree potential. Through the implementation of a self-consistent field, the single-electron wave functions can be calculated. Relatively early Hartree recognized that this method does not follow Pauli's exclusion principle because the resulting wave functions are not anti-symmetric. Therefore, Fock expanded it to the HF method by arranging the one-electron wave functions in the form of a Slater determinant:

$$\Psi(r_1, r_2, \ldots, r_N) = \frac{1}{\sqrt{n!}} \begin{vmatrix} \Psi_1(r_1) & \Psi_2(r_1) & \cdots & \Psi_N(r_1) \\ \Psi_1(r_2) & \Psi_2(r_2) & \cdots & \Psi_N(r_2) \\ \vdots & \vdots & \ddots & \vdots \\ \Psi_1(r_N) & \Psi_2(r_N) & \cdots & \Psi_N(r_N) \end{vmatrix}. \tag{3.7}$$

This approach conveniently uses the fact that a determinant is zero in the case when two identical rows or columns are present in the matrix. Thus, if electrons take up wave functions with the same spin, the wave function is identically equal to zero, and hence Pauli's exclusion principle is fulfilled [50]. In conclusion, the HF method is applicable to a small number of atoms but it is still impractical for bigger crystal structures. Moreover, it suffers some inaccuracies. The reason for that is the missing description of the repulsion of electrons due to the same charge. The most popular theory in computational materials science till today, Density Functional Theory (DFT), can handle this issue with a slightly different approach.

3.3 Density Functional Theory

In this section, the probably most powerful theory in computational materials science, namely Density Functional Theory (DFT), will be explained. As the topic is very complex, only the most important parts will be included. For further information and for deeper understanding, two selections from literature can be highly recommended [50, 54], which are also the basis for this section.

In general, DFT can be defined as a fully quantum-mechanical model for the solution of many-body problems by replacing the wave function formalism with the electron density. As claimed in the previous section, the many-body problem is solved by separating the motion of nuclei and electrons by the Born-Oppenheimer approximation. The advantage of the electron density approach subsequently lies in the fact that electron density does not depend on the number of electrons. Therefore the many-electron problem is solved automatically. The problem changes from a $3N$-dimensional equation to a N separate 3-dimensional one defining the electron density $n(r)$, which depends only on the location r.

3.3.1 Hohenberg and Kohn Theorems

The term DFT appeared for the first time in the 1960s, when Hohenberg and Kohn [55] conveyed their most important ideas with two theorems. These theorems try to link the electron density with the Hamiltonian operator, the wave function as well as with the external potential and, therefore, the system's properties. The most important finding is expressed via the first theorem:

1st Theorem of Hohenberg and Kohn:
The electron density $n(r)$ can uniquely characterize the ground-state of a many-body system contained in an external potential $U_{ext}(r)$.

The proof of this statement can be done by observing two electron systems with the same ground-state electron density. If these systems are related to different potentials, the potential difference between them will always be constant. Hence, $n(r)$ can be easily derived from wave functions Ψ or more precisely, from the probability of finding an electron at a certain position, $\Psi^*\Psi$ in a system of N electrons. It needs to be integrated over all coordinates but r_i:

$$n(r) = \sum_{i=1}^{N} \int \Psi^*(r, \ldots, r_N) \times \Psi(r, \ldots, r_N) dr_1 \ldots d_{i-1} \cancel{dr_i} dr_{i+1} \ldots dr_N. \tag{3.8}$$

Based on this outcome, an energy functional, the Hohenberg-Kohn functional, can be specified for the kinetic energy $\hat{T}_e$ and the Coulombic interactions between the electrons $\hat{U}_{e-e}$:

$$\hat{\mathcal{F}}[n(r)] = \hat{T}_e[n(r)] + \hat{U}_{e-e}[n(r)]. \tag{3.9}$$

This functional depends solely on $n(r)$. It is closely related to the corresponding energy terms in Eq. (3.4) of the HF method, but now exact results can be obtained for all electronic problems. Using the Hohenberg-Kohn functional, the second theorem of DFT can be formulated:

2nd Theorem of Hohenberg and Kohn:
The functional $\mathcal{F}[n(r)]$ is universal, and hence it is the same functional for all electronic systems. The ground state energy obtains its minimal value at the ground state density for any external potential $U_{ext}(r)$ and number of electrons N.

From this theorem, it can be realized that the ground state energy $\hat{E}[n(r)]$ of a system only depends on $n(r)$ and $U_{ext}(r)$ as:

$$\hat{E}[n(r)] = \hat{\mathcal{F}}[n(r)] + \int U_{ext}(r)n(r)dr. \tag{3.10}$$

The solution to this equation can be obtained with the variational principle, which means that a big set of different $n(r)$ gets inserted to find the minimum energy. However, no matter how big is the number of different tested $n(r)$, it cannot be taken for granted that ground state energy has been reached. To get full certainty, an additional approach has been established by Kohn and Sham.

3.3.2 Kohn-Sham Approach

In the Kohn-Sham approach [5], the Schrödinger equation is applied to a system of fictious non-interacting particles having the same density as the physical system. Consequently, the problem transforms into a one-electron eigenvalue problem and a set of single particle equations:

$$\hat{H}_{KS}\phi_i(r) = \epsilon_i\phi_i(r). \tag{3.11}$$

The resulting so-called Kohn-Sham orbitals, $\phi_i(r)$, describe the orbitals of the individual particles and define the electron density as:

$$n(r) = \sum_{i=1}^{N} |\phi_i(r)|^2. \tag{3.12}$$

The eigenvalues ϵ_i are the corresponding energies. The Kohn-Sham Hamiltonian, $\hat{H}_{KS}$, consists of the kinetic energy, $\hat{T}_0$, the classical electrostatic and the quantum-mechanical interactions between the electrons. With the previous assumptions, everything is described

without any approximations besides the quantum-mechanical effects. The system is described by non-interacting particles, therefore the effects between the mutually interacting electrons, namely exchange and correlation, are not explicitly present here. This remaining unknown piece of energy, the exchange-correlation potential, denotes the only approximation that has to be made in DFT.

3.3.3 Exchange-Correlation Potentials

The quantum mechanical effects involve two unknown energies that occur between electrons. The exchange of electrons denotes the repulsion between themselves originating from Pauli's principle. Correlation describes the electron-electron repulsion due to their same charge. These two effects are expressed by the exchange-correlation potential, U_{XC}, which is a critical contribution in a DFT run and hence needs to be as accurate as possible. The description of the corresponding energy is done via functionals, the most popular ones are the local density approximation (LDA) and the generalized gradient approximation (GGA). The simpler one is the LDA, which assumes that the exchange-correlation potential depends only on the electron density at a certain location of the electron system. This model fits only for systems with homogeneous electron gas. In other cases, inaccurate results are expected. It can be represented mathematically with the following integral:

$$\hat{E}_{XC}^{LDA}[n(r)] = \int n(r) U_{XC}(n(r)) dr. \tag{3.13}$$

A more accurate approach is GGA which also considers the gradient of the electron density. It takes inhomogeneities of the true charge density into account and therefore it is a better fit for real systems. It is defined as:

$$\hat{E}_{XC}^{GGA}[n(r)] = \int n(r) U_{XC}(n(r), \nabla n(r)) dr. \tag{3.14}$$

Different flavours of GGA, depending on their parametrization, exist. This means that exchange-correlation functionals get parametrized against big sets of experimental data to fit various properties. In solid states materials science, parametrization by Perdew, Burke and Ernzerhof (PBE or GGA-PBE) usually performs reliably and is often the first choice [5, 50, 56].

3.4 Implementation of DFT

3.4.1 VASP

The Vienna Ab initio Simulation Package (VASP) [6, 7] is a software toolkit for materials modelling at the atomic scale. It is capable of computing quantum mechanical ground-state properties within the framework of DFT from the first-principles. The program uses

projector-augmented wave (PAW) method [57] enabled pseudopotentials (PPs). These PAW-PPs specify the electron-nucleus interactions by splitting the overall wave function into a contribution of core electrons and one of valence electrons, which increases computational efficiency as well as accuracy. The valence electrons are additionally described by a plane wave basis set [58]. Matrix diagonalization schemes are used to get the electronic ground state at every molecular dynamics step with the free energy as the variational quantity. Four different input files, which fully determine the type and content of the VASP run, are required to set up a calculation. They always need to be named in the same way for every calculation:

- INCAR: Determines the objectives of a calculation and how it should reach them. It controls the run with a large number of parameters that can be set by means of tags. One important tag describes the cut-off energy (ENCUT), which defines the set size of functions (plane waves) that will be combined to describe the wave functions. A balance between accuracy and used computational power needs to be established, which can be estimated by convergence tests for each material. To guarantee a total energy accuracy of 1 meV/at., this value is used as the convergence criterion.

- KPOINTS: Samples the reciprocal k-space of a lattice, namely the first Brillouin zone. The electronic structure and other properties are only evaluated on these selected points. Speaking of accuracy, the chosen number of k-points complements the cut-off energy and also needs to be determined with the help of convergence tests. Several methods can be used to generate the grids, e.g. a Monkhorst-Pack [59], which generates the k-points evenly spaced throughout the first Brillouin zone.

- POSCAR: Contains the information about the lattice geometry and the type of species occupying the lattice sites. More precisely, this means that it contains the lattice vectors, the atomic positions and the allocation of elements to the positions. The number of atoms can be varied. For instance, supercells based on a unit cell can be generated with the special quasi-random structure (SQS) approach [60]. The scheme of SQS provides the best approximation of the real disordered state with a periodic supercell [61].

- POTCAR: Defines the PPs of each element that is included in the calculation. PPs describe the wave functions of the active valence electrons in an imitative way, whereas the core electrons are freezed together with the nucleus. This reduces the number of electrons and increases the efficiency of the calculations. For alloys, the POTCAR files of each element need to be combined in the right order according to the POSCAR file. The projector augmented wave potentials together with the parametrized exchange-correlation potentials are included in this file.

The package is most efficient when compiled on high-performance computing (HPC) clusters. For example, the *Vienna Scientific Cluster* (VSC) and a less powerful one, which is available at *Montanuniversität Leoben*, can be used. For further information, the following literature is recommended [7, 50, 62].

3.4.2 EMTO

Another code which implements the DFT, is the Exact Muffin-Tin Orbital (EMTO) code. EMTO is an all-electron method based on so-called muffin-tin orbitals to solve the Kohn-Sham equations. Combined with the Coherent Potential Approximation (CPA), it provides a computationally very efficient tool to treat disordered systems such as HEAs. Muffin tin orbitals describe the spherical potentials at the lattice sites of a structure as well as the constant potentials in their interstitial regions. The EMTO formalism is an improvement of the original muffin-tin orbital method because it calculates the exact single electron potentials. It is based on Green's function, which contains all the information about the electronic system and therefore replaces the Hamiltonian for solving the Schrödinger equation. Additionally, the CPA demonstrates a single-site approximation, where the potential of a disordered alloy is substituted by an ordered effective medium. Each alloy component receives a single-site Green's function, and their average leads to a coherent potential, which possesses the symmetry of the corresponding crystal lattice. Hence, a monoatomic setup is sufficient for the calculation of ground state energies of complex disordered alloy systems, which makes this method computationally very efficient. Within EMTO-CPA, all the structural parameters are fixed, and no relaxation processes occur, which is often stated as a disadvantage. The method is described more in detail in *Levente Vitos'* book, who implemented this approach [63].

Chapter 4

Results and Discussion

In general, two HEAs, TiAlNbV-Mo and TiAlNbV-Mn, are tested on their phase stability. This is done on the one hand directly from the DFT calculations at 0 K and on the other hand also by introducing temperature effects. These effects are implicitly included by the configurational entropy and subsequently also by the vibrational entropy estimated via the Debye model. To get information about phase stability, mixing enthalpies of all the possible decomposition products are calculated and compared. The results of the VASP calculations are also partly checked against the results calculated with the EMTO method. Experimental results for comparison have been provided by colleagues [12].

4.1 Approach and Computational Details

Due to the huge amount of elemental combinations, an experimental investigation of HEAs is hardly feasible. Therefore, atomistic modelling, together with first-principles calculations, is often used to tackle such problems. Within this thesis, the two studied HEAs are studied against decompositions using all possible decomposition routes containing unaries, binaries, ternaries and quaternaries. These products and the five-component HEA (quinary) are fully relaxed regarding the atomic positions, cell shape, and volume (INCAR-tag: `ISIF = 3`) of the structures to obtain the ground-state total energies. within this thesis, all first-principles calculations are done with VASP [6, 7] unless indicated differently. The electron-ion interactions are described with projector augmented wave pseudopotentials. The exchange and correlation effects are treated at a generalized gradient approximation level as parametrized by Perdew, Burke and Ernzerhof (GGA-PBE [5, 56]). To ensure the accuracy of 1 meV/at. or better, plane-wave cut-off energy (ENCUT) of 400 eV was used for all the calculations. A k-point mesh was automatically generated to sample the irreducible wedge of the Brillouin zone by using the Monkhorst-Pack scheme and a length input parameter of 60.

To model all the considered systems, one-atomic primitive BCC unit cells ($a = b = c$, $\alpha = \beta = \gamma = 109.47°$) of the pure metals are used for the generation of SQS supercells containing up to 125 atoms. The supercells have been generated from the relaxed unit cells via a tool developed by Dominik Gehringer, the *sqsgenerator* [64]. The requirement of equiatomic compositions leads to the supercell sizes summarized in Tab. 4.1. The FCC and HCP-C14 structures are generated in a similar way by using the *sqsgenerator*, whereas the number of atoms and cell size of the HCP-C14 supercells can differ due to a two-atomic basis of the unit cell.

Table 4.1: Supercell sizes of the investigated systems.

System	Supercell Size	Number of Atoms
Unary	$1 \times 1 \times 1$	1
Binary	$4 \times 4 \times 4$	64
Ternary	$5 \times 4 \times 3$	60
Quaternary	$4 \times 4 \times 4$	64
Quinary (HEA)	$5 \times 5 \times 5$	125

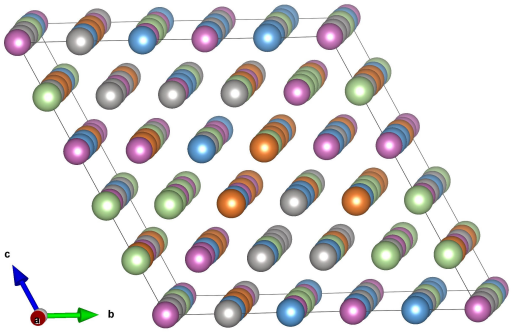

Figure 4.1: The TiAlNbV-Mo HEA in a $5 \times 5 \times 5$ primitive BCC SQS supercell with 125 atoms.

Out of all possible decomposition routes, we consider only those consisting of decomposition products with equiatomic compositions, as demonstrated in Fig. 4.2. By using the example of TiAlNbV-Mo, it is shown that the HEA can decompose in unary+quaternary, binary+ternary and binary+binary+unary systems. The elements order randomly within the products. This leads to certain limitations in order to allow for reasonable evaluations. Firstly, each element is contained only in one decomposition product and secondly, each product has to remain in equiatomic composition. In general, the HEAs are studied extensively in the BCC phase because literature predicts it as the dominant phase for this

elemental composition [10]. In the first place, it is assumed that the possible products also precipitate as BCC phases. In the following studies, the hexagonal close-packed (HCP) C14 phase is also included as a potential decomposition product of the TiAlNbV-Mn alloy it has been experimentally reported that this phase is very likely to form if Mn is combined with TiAl. To complete the possible decomposition scenarios, the systems are also studied as a simple FCC phase.

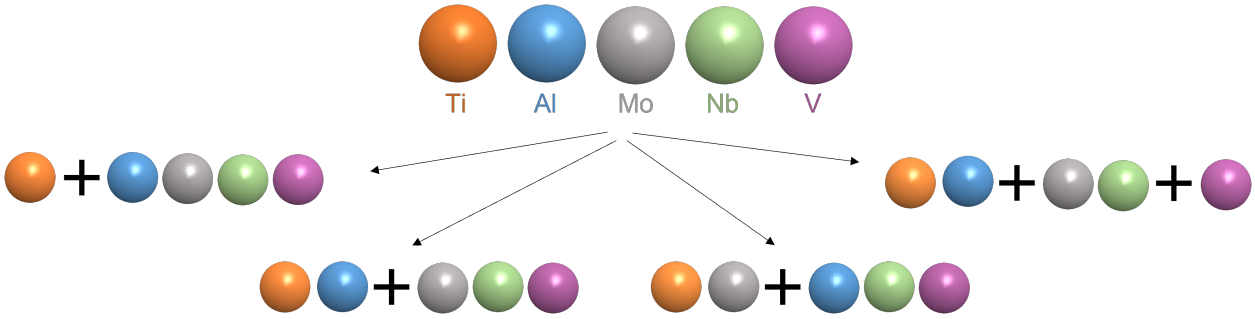

Figure 4.2: Considered decomposition routes with TiAlNbV-Mo HEA as an example.

4.2 Mixing Enthalpies of BCC HEAs and their BCC Decomposition Products

Total ground-state energies are obtained from DFT calculations for the HEAs as well as for their decomposition products. The mixing enthalpies are calculated from the total ground-state energies for every alloy using Eq. (2.4). In general, DFT operates at $T = 0\,\mathrm{K}$, which means that ΔH_{mix} is equal to the Gibbs free energy ΔG_{mix} (see Eq. (2.1)). Therefore, similar requirements (values lower than zero lead to stable structures and higher than zero to decomposition) can be applied for ΔH_{mix} at zero temperature. All values are calculated with respect to unary reference states (see e.g. Tab. 2.1). Fig. 4.3 shows the ΔH_{mix} of TiAlNbV-Mo and TiAlNbV-Mn together with their considered decomposition products. The ΔH_{mix} of both HEAs are put in one graph as they are only differing by the products, which contain Mn or Mo. Most of the alloys seem to be stable with respect to their unary elements, as their ΔH_{mix} results in a negative value. This means, that there exist several combinations of elements, which can definitely form a phase or rather would be able to precipitate from the HEA. Just a few alloys, such as NbV, TiV, MnNb and TiNbV, are not expected to form after the decomposition from the BCC phase HEA, as they do not form stable solid solutions themselves (positive mixing enthalpies). Interestingly, TiAl exhibits the lowest mixing enthalpy of all binaries, which is in accordance with the knowledge that a mixture of these two elements can lead to several different intermetallic phases [9]. In general, all alloys containing Al exhibit a much lower ΔH_{mix} than those without Al. This agrees with

the postulation in Sec. 2.2.4 that Al builds very strong bonds with other elements and thus promotes the formation of BCC phases. The slightly negative ΔH_{mix} of the HEAs, TiAlNbV-Mo and TiAlNbV-Mn, imply that they are also stable with respect to their unary states at zero temperature. However, from these results, it can be estimated that the single-phase BCC HEAs may not persist at high temperatures as there already exist many candidates for decomposition products.

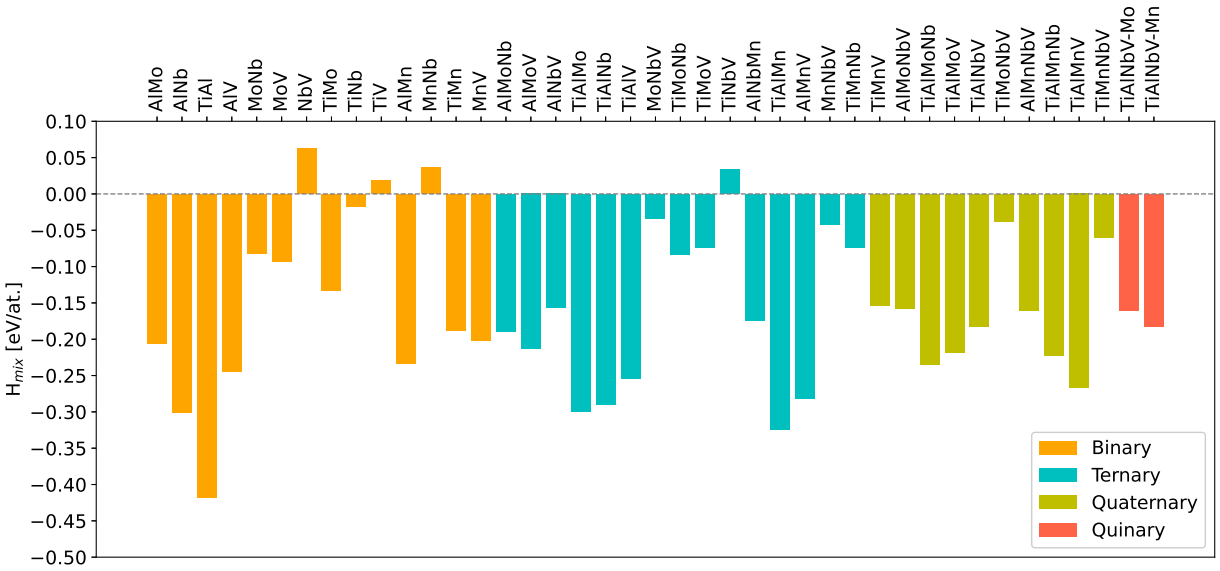

Figure 4.3: Comparison of the mixing enthalpies ΔH_{mix} of the BCC HEAs, TiAlNbV-Mo and TiAlNbV-Mn, as well as their corresponding BCC decomposition products.

By considering the quaternaries, it can be assumed that TiAlMoNb+V and TiAlMnV+Nb are possible decomposition routes as TiAlMoNb and TiAlMnV exhibit very low ΔH_{mix} compared to the others. Within the ternary systems, TiAlNb, TiAlMo and TiAlMn have the most negative values. However, the probability that the HEAs decompose into TiAlMo+NbV or TiAlMn+NbV is relatively low due to the positive ΔH_{mix} of NbV and therefore the HEA will be most likely the more stable system in both cases. On the other hand, already from here it can be seen that TiAlNb+MoV represents a decomposition route with high driving force for decomposition, which will be also confirmed in the next sections. Lastly, as TiAl exhibits the lowest ΔH_{mix}, it is very likely to decompose together with MnNbV or MoNbV. The high configurational entropy of HEAs is the force working against decomposition, which we will be introduced in the next part of the thesis.

4.3 Phase Stability of BCC HEAs including Configurational Entropy

We now discuss the influence of the configurational entropy on the phase stability of the HEAs. This information is provided by ΔG_{mix} at a temperature unequal 0 K. The consequence of finite temperature is that the entropy term is now included as well, as stated in Eq. (2.1). The configurational contribution constitutes the biggest contribution to the total entropy when treating HEAs (at least at moderate temperature ranges) and, therefore, should be a good starting point for discussing temperature effects. Consequently, this chapter considers solely the configurational contribution, which is calculated with Eq. (2.5). Subsequently, ΔG_{mix} is obtained via Eq. (2.6), with which the driving forces for decomposition of the HEAs at different temperatures can be estimated easily. A minor role in stability plays the volume change ΔV during decomposition, which, nevertheless, will also be discussed shortly. Its contribution is expressed by Eq. (2.7).

4.3.1 Phase Stability of TiAlNbV-Mo for BCC+BCC Decomposition

We start by focusing on the TiAlNbV-Mo HEA, which is assumed to consist of a BCC structure. The corresponding decomposition products are also regarded as BCC phases. Table 4.2 presents the five decomposition routes with the highest driving force for decomposition at 500 K, 1000 K and 1200 K. The magnitude of the driving force is ranked for the values of ΔG_{mix}. The red numbers indicate positive ΔG_{mix} and therefore, the HEA being unstable w.r.t. that particular decomposition route. Green numbers indicate a stabilization of the HEA due to the increased temperature. The decomposition route with the highest ΔG_{mix} exhibits the highest probability for decomposition. In addition, the ΔV is indicated, which contributes to the elastic stabilization.

At 500 K the HEA is predicted to be unstable because of the positive ΔG_{mix} of the two decomposition routes, namely to TiAlNb+MoV and TiAlMoNb+V. Therefore, it is assumed that the TiAlNbV-Mo alloy will not stay in a single-phase BCC alloy at this temperature, provided that it has enough time to reach its equilibrium. By heating up the alloy, the effect of the configurational entropy is more and more pronounced. Hence, the HEA becomes more stable at increased temperatures, which can be clearly seen through the negative ΔG_{mix} of the decomposition routes with the highest driving force at 1000 K and 1200 K. As a consequence, the TiAlNb+MoV route does not exhibit the tendency to facilitate the dissociation in BCC products anymore; instead, it is more likely that the HEA maintains its single-phase BCC structure. Moreover, the ΔG_{mix} at 1200 K is much more negative than at 1000 K, which again clearly shows the impact of the entropy, especially of the configurational contribution.

The last column of the table shows the volume difference, ΔV, between the HEA and

Table 4.2: Predicted routes with highest driving force for BCC → BCC + BCC decomposition at different temperatures. Red numbers indicate positive ΔG_{mix} and green numbers negative values, which refers to higher stability of the HEA.

Temperature (K)	Decomposition Route	ΔG_{mix}(eV/at.)	ΔV (-)
500	TiAlNb + MoV	0.0219	0.0059
	TiAlMoNb + V	0.0055	0.0035
	TiAl + MoV + Nb	-0.0016	0.0022
	TiAl + MoNbV	-0.0019	0.0020
	TiAlV + MoNb	-0.0043	-0.0002
1000	TiAlNb + MoV	-0.0071	0.0059
	TiAlMoNb + V	-0.0160	0.0035
	TiAlMoV + Nb	-0.0293	0.0022
	TiAl + MoNbV	-0.0309	0.0020
	TiAlV + MoNb	-0.0333	-0.0002
1200	TiAlNb + MoV	-0.0187	0.0059
	TiAlMoNb + V	-0.0246	0.0035
	TiAlMoV + Nb	-0.0379	0.0022
	TiAl + MoNbV	-0.0425	0.0020
	TiAlV + MoNb	-0.0449	-0.0002

its corresponding decomposition products. ΔV is based on the relaxed structures at 0 K, and hence this stabilization mechanism does not exhibit temperature dependence (in our simplified treatment). A volume increase is predicted after the decomposition of the HEA in majority of cases, which leads to a stability gain of the HEA. However, these changes in volume turn out to be very small (mostly $\Delta V < 1\,\%$). The reason for the low ΔV is based on the presumption that the products only decompose into BCC phases. So, no high-volume phases like a wurtzite structure, that would exceed the volume of a cubic phase by $\approx 20\,\%$ [36], has been taken in account. Moreover, from results of Kretschmer *et al.* [36] it can be estimated that the stabilization by ΔV takes effect from values higher than $\approx 6\,\%$, which are not reached within our systems. In reality the most stable structures of the decomposition products can deviate from BCC and therefore the formation of high-volume phases would be possible. Nevertheless, within this study the impact of ΔV on the stability is estimated as marginal due to the sole consideration of BCC decomposition products and will not be treated any further.

In conclusion, the results in Tab. 4.2 reveal that the TiAlNbV-Mo HEA has the potential to form a single-phase BCC alloy due to the stabilization through entropy at high temperatures. However, a risk exists that the HEA decomposes into brittle BCC phases by cooling it down as ΔG_{mix} already turns positive at 500 K. The reader is reminded that some approximations still needed to be done in the calculations; nevertheless, the results provide the first hint

of whether it is even possible to form a stable HEA with certain elements or not. The results in the table manifest the assumption that TiAlNbV-Mo possesses a high potential to accomplish the requirements for a single-phase BCC HEA.

4.3.2 Phase Stability of TiAlNbV-Mn for BCC+BCC Decomposition

In this section, we perform an analogous analysis to the previous section, this time for the TiAlNbV-Mn HEA. To start with, the HEA, as well as the decomposition products, are considered to consist of BCC phases. Table 4.3 summarizes the decomposition routes with the highest driving force for decomposition together with their ΔG_{mix} and ΔV values.

Table 4.3: Predicted routes with highest driving force of the TiAlNbV-Mn system for the BCC $\rightarrow$ BCC + BCC decomposition at different temperatures. Red numbers indicate positive ΔG_{mix} and green numbers negative values, which refers to higher stability of the HEA.

Temperature (K)	Decomposition Route	ΔG_{mix}(eV/at.)	ΔV (-)
500	TiAlNb + MnV	0.0435	0.0058
	TiAl + MnV + Nb	0.0200	0.0018
	TiAlMnV + Nb	-0.0016	0.0098
	TiMnV + AlNb	-0.0019	0.0009
	TiAl + MnNbV	-0.0043	-0.0186
1000	TiAlNb + MnV	0.0145	0.0058
	TiAlMnV + Nb	-0.0118	-0.0084
	TiAl + MnV + Nb	-0.0254	0.0018
	TiMnV + AlNb	-0.0281	0.0009
	TiAl + MnNbV	-0.0476	0.0036
1200	TiAlNb + MnV	0.0029	0.0058
	TiAlMnV + Nb	-0.0204	-0.0084
	TiMnV + AlNb	-0.0397	0.0009
	TiAl + MnV + Nb	-0.0436	0.0018
	TiAlMnNb + V	-0.05644	-0.0006

The decomposition route, namely the TiAlNb+MnV route, exhibiting the highest driving force for decomposition remains positive up to 1200 K. Consequently, not even the configurational entropy at high temperatures can compensate for the instability of the TiAlNbV-Mn BCC HEA. The value of ΔG_{mix} for TiAlNb+MnV is reduced close to zero at 1200 K; nevertheless, an even higher temperature is necessary to obtain a single phase BCC HEA. However, this would lead to temperatures close to the melting point, which is not reasonable anymore. Interestingly, the TiAl+MnV+Nb route, which has the second highest driving force at 500 K, rapidly decreases G_{mix} with increasing temperature. It even "queues up" behind TiAlMnV+Nb and TiMnV+AlNb at 1200 K and therefore experiences much faster stabilization. The reason for this incidence is the higher overall configurational entropy of

the three component decomposition route compared to the routes containing only two products. Thereby, the impact of temperature is bigger for decomposition routes with a higher number of products. A more detailed analysis of this faster stabilization as well as the configurational entropy can be found in Appendix B. Finally, the conclusion can be drawn that the TiAlNbV-Mn HEA is not expected to form a stable single-phase BCC alloy and will most likely dissociate in TiAlNb+MnV due to its instability up to 1200 K.

4.3.3 Phase Stability of TiAlNbV-Mn for BCC+C14 Decomposition

From experimental observations 4.5 as well as former studies on TiAl [15], we know that the combination of TiAl and Mn shows the tendency to precipitate an HCP phase, namely the C14 Laves phase. Therefore, the ground state energies, as well as mixing energies were calculated also for this phase for all decomposition products (containing Mn) and evaluated together with the BCC structures. Hence, for the BCC TiAlNbV-Mn HEA not only BCC+BCC, but also BCC+C14 decomposition routes are considered. The results for this scenario are summarized in Tab. 4.4, including also the information on the corresponding phases.

Table 4.4: Predicted routes with highest driving force of the TiAlNbV-Mn system for BCC → BCC + C14(HCP) decomposition at different temperatures. Red numbers indicate positive ΔG_{mix} and green numbers negative values, which refers to higher stability of the HEA.

Temperature (K)	Decomposition Route	Phase	ΔG_{mix}(eV/at.)	ΔV (-)
500	TiAl + MnNbV	BCC + C14	0.0759	0.0102
	TiAlNb + MnV	BCC + C14	0.0190	0.0165
	TiAl + MnV + Nb	BCC + C14 + BCC	-0.0045	0.0126
	TiMnNb + AlV	C14 + BCC	-0.0117	0.0013
	TiAlNb + Mn + V	BCC + C14 + BCC	-0.0490	0.0130
1000	TiAl + MnNbV	BCC + C14	0.0470	0.0102
	TiAlNb + MnV	BCC + C14	-0.0100	0.0165
	TiMnNb + AlV	C14 + BCC	-0.0407	0.0013
	TiAl + MnV + Nb	BCC + C14 + BCC	-0.0499	0.0126
	TiAlNbV + Mn	BCC + C14	-0.0791	0.0146
1200	TiAl + MnNbV	BCC + C14	0.0354	0.0102
	TiAlNb + MnV	BCC + C14	-0.0216	0.0165
	TiMnNb + AlV	C14 + BCC	-0.0523	0.0013
	TiAl + MnV + Nb	BCC + C14 + BCC	-0.0681	0.0126
	TiAlNbV + Mn	BCC + C14	-0.0878	0.0146

The outcome of this investigation is similar to the BCC+BCC decomposition routes. At 1200 K the HEA is still expected to be unstable because of the positive ΔG_{mix} of TiAlNb+MnV and therefore, it is again likely that the TiAlNbV-Mn HEA decomposes. The phases of these

products are BCC TiAl and HCP-C14 MnNbV. This further underlines the previous result that no stable BCC HEA for TiAlNbV-Mn will form.

However, for the BCC+C14 decomposition routes, the effect of ΔV is more pronounced. In comparison to the previous results of ΔV, a factor 2-3 high values are calculated, and therefore the decomposition driving force for this HEA correspondingly decreases. These values are obtained due to the higher volume of the HCP phase relative to the BCC phase. Nevertheless, the influence is estimated as marginal, because the change is still only around 1.5 %.

It is expected that Mn increases the driving force for precipitation of the HCP-C14 phase. Hence, we investigate the BCC and the HCP TiAlNbV-Mn systems with a varied amount of Mn, compensated by the content of Ti. Fig. 4.4 presents the resulting mixing enthalpies ΔH_{mix} for increasing Mn content with respect to unaries. Alloys only can form a solid solution if ΔH_{mix} is negative. The figure shows that the mixing enthalpy of the BCC phase is almost independent of the increased Mn and the simultaneous decrease of Ti content. On the contrary, the HCP-C14 phase shows a clear trend to lower values of enthalpy and even to negative values with increasing Mn fraction.

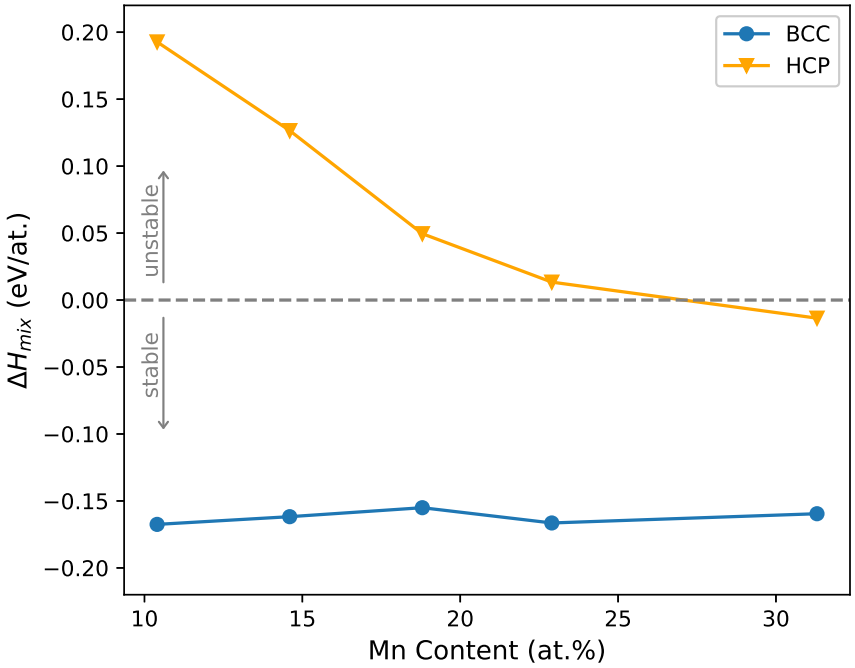

Figure 4.4: Mixing Enthalpy ΔH_{mix} for the HCP-C14 phase and the BCC phase as a function of Ti and Mn content in $Ti_{0.4-x}Al_{0.2}Nb_{0.2}V_{0.2}Mn_x$.

The C14 phase has a higher probability of forming with the addition of Mn; nevertheless, BCC single-phase solid solution remains the more stable phase. The results presented in this section thus lead to a conclusion that Mn does not turn out to be the proper element for a

stable TiAl-based HEA, because the formation of the HCP-C14 phase can probably not be suppressed. This is also confirmed by experimental observations, in which our experimental colleagues found that a TiAlNbV-Mn HEA with decreased Mn content and increased Ti content has much more potential for a single-phase BCC HEA (see Sec. 4.5).

4.3.4 Comparison with EMTO-CPA for BCC+BCC Decomposition

The following results were also obtained with DFT, but this time implemented in the EMTO code. EMTO combined with coherent potential approximation (CPA) constitutes a tool which is very useful for complex disordered systems such as HEAs (see Sec. 3.4.2). In turn, HEAs are a proper showcase to test this method against the results of phase stability predicted using VASP-SQS. The initial structures for the EMTO calculations are generated with the ground state lattice parameters of the VASP-SQS calculations.

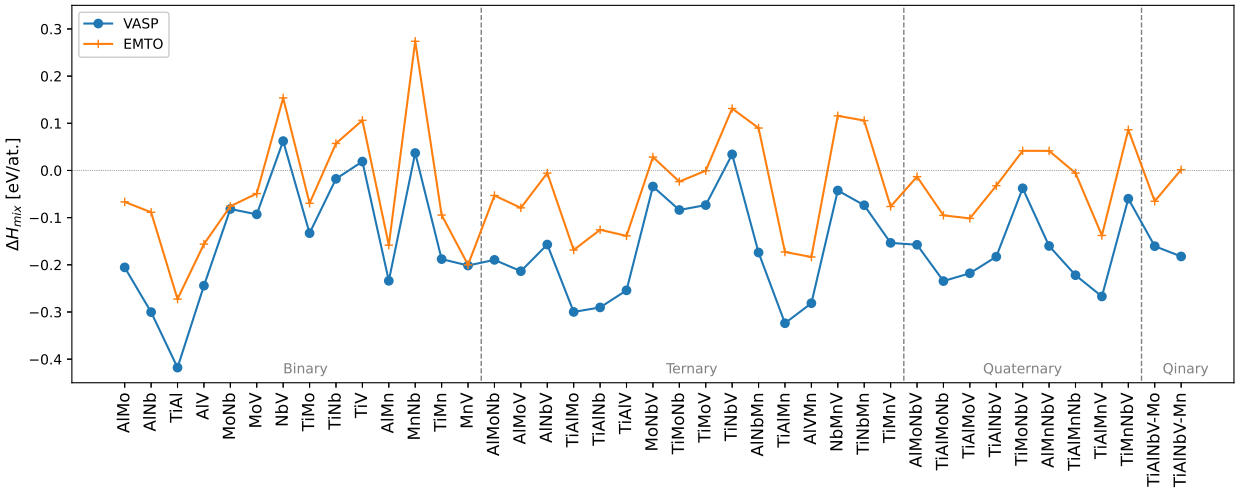

Figure 4.5: Comparison of the mixing enthalpies obtained by first-principles calculations ($T = 0\,\mathrm{K}$) with VASP and EMTO. The results for TiAlNbV-Mo and TiAlNbV-Mn as well as for their corresponding decomposition products are plotted.

For the case of TiAl-HEAs, the obtained energies from EMTO are very satisfying as the values of ΔH_{mix} of most decomposition products are close to the VASP results (Fig. 4.5). There are only a few exceptions, for which the difference is somewhat larger or VASP predicts negative ΔH_{mix} and while EMTO positive values. The systems exhibit a gap of $\approx 0.1\,\mathrm{eV/at.}$ between the ΔH_{mix} obtained by two methods in average. By observing the binary, ternary and quaternary systems individually, the mean differences are slightly increasing with a higher number of elements. The deviations can be assigned to the relaxation processes happening in the VASP runs but not accounted for in the EMTO calculations. In this sense, the fact that the VASP results yield lower (more negative) ΔH_{mix} can be fully ascribed to this phenomenon.

Based on this satisfactory agreement between the results obtained by the EMTO-CPA and VASP-SQS methods, the EMTO ground state energies are further analysed with respect to the phase stability of the TiAlNbV-Mo and TiAlNbV-Mn HEAs. We apply the same methodology as in Sec. 4.3 just by using the EMTO energies this time, which leads to the results in Tab. 4.5. Here, the ΔG_{mix} is again calculated by Eq. 2.6 and the decomposition routes are ranked according to the highest driving forces for the decomposition.

Table 4.5: Predicted routes with highest driving force for BCC → BCC + BCC decomposition at different temperatures calculated with EMTO-CPA method. Red numbers indicate positive ΔG_{mix} and green numbers a change to negative values.

	Temperature (K)	Decomposition Route	ΔG_{mix}(eV/at.)	ΔV (-)
TiAlNbV-Mo	500	TiAl + MoNb + V	0.0286	0.0026
		TiAlV + MoNb	0.0193	-0.0028
		TiAl + MoV + Nb	0.0179	0.0072
		TiAlNb + MoV	0.0007	0.0144
		TiAl + MoNbV	-0.0023	0.0064
	1200	TiAlV + MoNb	-0.0213	-0.0028
		TiAl + MoNb + V	-0.0350	0.0026
		TiAlMoV + Nb	-0.0357	-0.0029
		TiAlNb + MoV	-0.0399	0.0144
		TiAlMoNb + V	-0.0409	0.0019
TiAlNbV-Mn	500	TiAl + MnV + Nb	0.1452	0.0080
		TiAlNb + MnV	0.1280	0.0158
		TiAlMnV + Nb	0.0903	-0.0151
		TiAlMnV + Nb	0.0717	0.0248
		AlMnV + Nb + Ti	0.0707	-0.0038
	1200	AlNbTi + MnV	0.0875	0.0158
		AlTi + MnV + Nb	0.0816	0.0080
		AlMnTiV + Nb	0.0602	-0.0151
		AlMnV + NbTi	0.0192	-0.0105
		AlMnV + Nb + Ti	0.0135	-0.0038

For TiAlNbV-Mo at 500 K, four different products exhibit a driving force for the decomposition of the HEA. However, all ΔG_{mix} values become negative and the HEA is stabilized when the temperature increases to 1200 K. The same behaviour has been observed for BCC TiAlNbV-Mo in the VASP-SQS results. Moreover, also the decomposition routes are the same or very similar, just the order in the table has slightly changed.

In contrast, the results of the TiAlNbV-Mn HEA immediately imply that this HEA will not form as a single phase BCC alloy due to the positive ΔG_{mix} values. This is in accordance with the VASP results, which also predicted the TiAlNbV-Mn to be unstable. The larger values

of ΔG_{mix} can be again ascribed to the missing relaxation processes in EMTO. However, the core statement of the results about the phase stability yields the same conclusion and therefore strengthens the results obtained by VASP.

4.4 Stabilization Effect of Vibrational Entropy - Debye Model

Until now, only the configurational entropy, which is presumed to have the biggest contribution to the total entropy of HEAs, has been included in the evaluations of the phase stability. This section aims to estimate the impact of another entropic contribution, the vibrational entropy, on the stability of the HEAs.

Vibrational effects are evaluated with the harmonic Debye model and expressed by the vibrational free energy as described in Sec. 2.6. We consider the decomposition products with the highest driving force for decomposition taken from the results, where only the configurational entropy was considered (Sec. 4.3). The Debye model (Sec.2.6) is then applied to the involved systems, the decomposition products as well as HEAs. The focus is laid on whether the vibrational entropy contribution has such an impact that it can potentially stabilize the TiAlNbV-Mo and TiAlNbV-Mn HEAs. The considered decomposition routes are namely TiAlNb+MoV, TiAlMoNb+V, TiAl+MoV+Nb, TiAlNb+MnV, TiAlMnV+Nb and TiAl+MnV+Nb, in which all the products are considered as BCC phases.

4.4.1 Elastic Properties of BCC HEAs and Decomposition Products

As the vibrational characteristics of a material are closely related to the elastic properties, the elastic constants and moduli of the systems need to be calculated. This has been done by the stress-strain method (Sec. 2.7). Table 4.6 lists all the gained C_{ij} values for the cubic systems as well as the corresponding Young's moduli E, shear moduli G and bulk moduli B for the investigated decomposition products.

The results for C_{ij} suggest that all systems are mechanically stable as they fulfil the criteria of Born and Huang [65]:

$$C_{11} + 2C_{12} > 0, \quad C_{11} - |C_{12}| > 0, \quad C_{44} > 0. \tag{4.1}$$

Especially MoV and MnV form very stiff BCC phases as they exhibit very high C_{11}, E and also B compared to the other alloys. A scan through Young's moduli shows that solid solution strengthening takes effectively place as the pure elements have the lowest E. The HEAs exhibit lower moduli than most of the other systems, and hence no effect due to solid solution strengthening can be observed.

The important quantity for the following evaluations is the bulk modulus. To prove the correctness of the obtained results from the stress-strain method, the moduli of the pure

Table 4.6: Calculated elastic constants and moduli for the HEAs and their decomposition products with the highest driving force for decomposition.

Material System	C_{11} (GPa)	C_{12} (GPa)	C_{44} (GPa)	E (GPa)	G (GPa)	B (GPa)
Nb	246	136	16	77	27	169
V	274	144	23	100	35	185
TiAl	199	98	73	163	63	132
MoV	374	152	57	201	74	225
MnV	422	150	85	270	103	241
TiAlNb	170	129	68	115	142	139
TiAlMoNb	208	142	70	140	52	163
TiAlMnV	235	136	84	180	68	169
TiAlMoNbV	219	144	61	138	50	169
TiAlMnNbV	206	136	61	134	49	159

metals are compared to values found in the Materials Project database [66]. It reports bulk modulus of 167 GPa obtained for Nb BCC [67] (here: 169 GPa) and 179 GPa for V BCC [68] (here: 185 GPa), which clearly shows that our results are reasonable and accurate enough to apply them to the Debye model.

4.4.2 Interpretation of Vibrational Free Energy

With the knowledge of the bulk modulus, the vibrational free energy F_{vib} can be determined by following the scheme from Sec. 2.6 beginning with Eq. 2.12. Fig. 4.6 demonstrates the trends for the vibrational free energies with increasing temperature. All energies turn more negative by raising the temperature. The lowest values are obtained by the pure metals, especially by Nb, which is about 0.1 eV/at. lower than the HEAs and shows a much steeper slope. This can be associated with the high molar mass of Nb as the vibrations are energetically much more pronounced due to this effect. MnV constitutes the alloy with the highest (least negative) F_{vib} that probably originates from its very high stiffness indicated by the high E and B. TiAlMnV and TiAl also exhibit high values of energy, although they only have moderate or even low bulk moduli; the reason for the high F_{vib} could come from their relatively low averaged molar mass. The two HEAs exhibit average values of F_{vib} and lie in the middle of the evaluated systems.

4.4.3 Transition Temperature for the Stabilization of HEAs

Using the vibrational free energies, Gibb's free energy ΔG_{mix} can be reevaluated by using Eq. 2.16. This is done for steps of 100 K ranging from 500 to 1200 K, as it is presented for the decomposition routes of TiAlNbV-Mo in Fig. 4.7. The obtained data points are fitted with a linear function so that the transition temperature from a stable to an un-

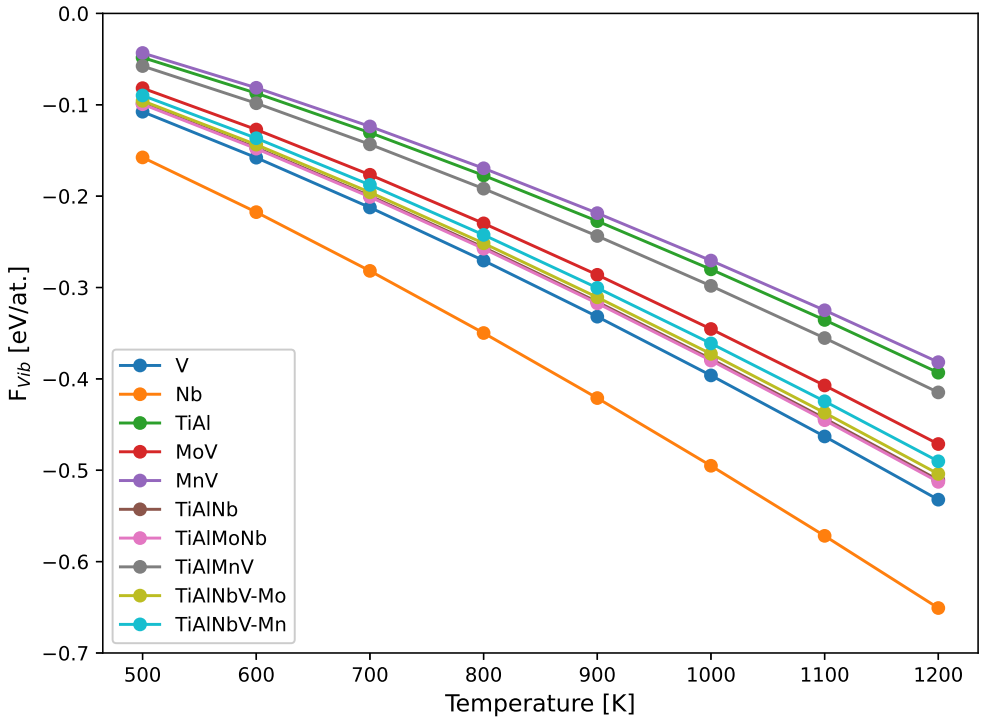

Figure 4.6: Vibrational free energies of the BCC HEAs and decomposition products with the highest driving force for decomposition as calculated by the harmonic Debye model.

stable HEA can be estimated. This is indicated by the crossover with the zero-line. The inclusion of the vibrational effects leads to a reduction of the ΔG_{mix} for the TiAlNb+MoV and TiAl+MoV+Nb decomposition routes. Consequently, this partly stabilizes (acts along with the configurational entropy) the HEA and pushes the transition temperature T_{trans}, at which the HEA gets stable, down. For instance, the TiAlNb+MoV route reduces its transition temperature by ≈100 K and therefore is predicted to be stable already at 776 K. Similarly, TiAl+MoV+Nb reaches its stability at 500 K, but with the consideration of F_{vib}, ΔG_{mix} is reduced even further and is stable down to 360 K. Nevertheless, the impact is not huge enough to obtain a stable single-phase BCC HEA at room temperature. An opposite behaviour is observed for the TiAlMoNb+V route. Here, the HEA gets destabilized by including the vibrational entropy contribution. This unexpected destabilization can occur because the F_{vib} is strongly negative for the decomposition products. Consequently, the decomposition becomes energetically even more favoured after the inclusion of the lattice vibrations. This particular example nicely demonstrates that contrary to the configurational entropy, the addition of the vibrational entropy does not always lead to a stabilization of the HEA, but can also destabilize it for certain decomposition routes. Hence, the transition temperature from unstable to stable TiAlNbV-Mo HEA has not decreased significantly. This comes from destabilization of the TiAlMoNb+V route, which implies a temperature difference of more than +200 K compared to the situation without vibrational effects and leads to

a transition temperature of 833 K. Finally, the consideration of the vibrational entropy leads

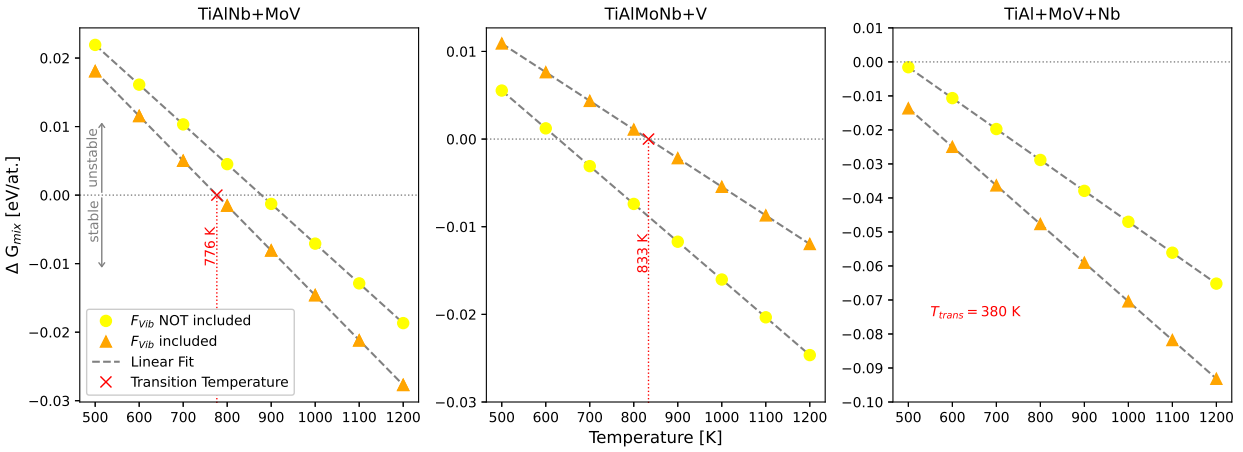

Figure 4.7: Estimated stabilization impact of the vibrational free energy on the HEAs demonstrated by the change of Gibb's free energy of the decomposition routes with the highest driving force for decomposition of TiAlNbV-Mo. The red crosses and temperatures indicate the transition temperatures from unstable to stable after including the vibrational free energy (orange values). If there is no cross as indicator, the transition temperature decreased to a value, which is out of the x-range.

to the awareness that no thermodynamically stable single phase BCC HEA can be obtained at temperatures below ≈ 800 K, although the total stability threshold shifts to slightly lower temperatures.

Similarly, ΔG_{mix} is also recalculated for the decomposition routes with the highest driving force for decomposition of the TiAlNbV-Mn HEA. These results are plotted in Fig. 4.8. In contrast to the TiAlNbV-Mo HEA system, the effect of vibrational entropy is much more pronounced for most of the decomposition routes. This is particularly true for the TiAlNb+MnV as well as for TiAlMnV+Nb routes. The TiAlNb+MnV route exhibits positive ΔG_{mix} at 1200 K by considering solely the configurational entropy. With the addition of the vibrational entropy, it crosses to negative values already at around 860 K. TiAlMnV+Nb is even more affected as the HEA is already predicted as stable at 500 K and even down to 360 K by including F_{vib}. Interestingly, the second decomposition route, TiAl+MnV+Nb is more or less not affected by the additional temperature effects and shows only minor changes. However, the conclusion of the results again is that still no fully stable BCC HEA can be obtained, although the stable region (at least with respect to BCC → BCC + BCC decompositions) shifts to significantly lower temperatures (from above 1200 K to below 900 K). To have a better overview, how F_{vib} changed the stability of the HEAs in terms of transition temperatures, these temperatures are summarized in Tab. 4.7 again.

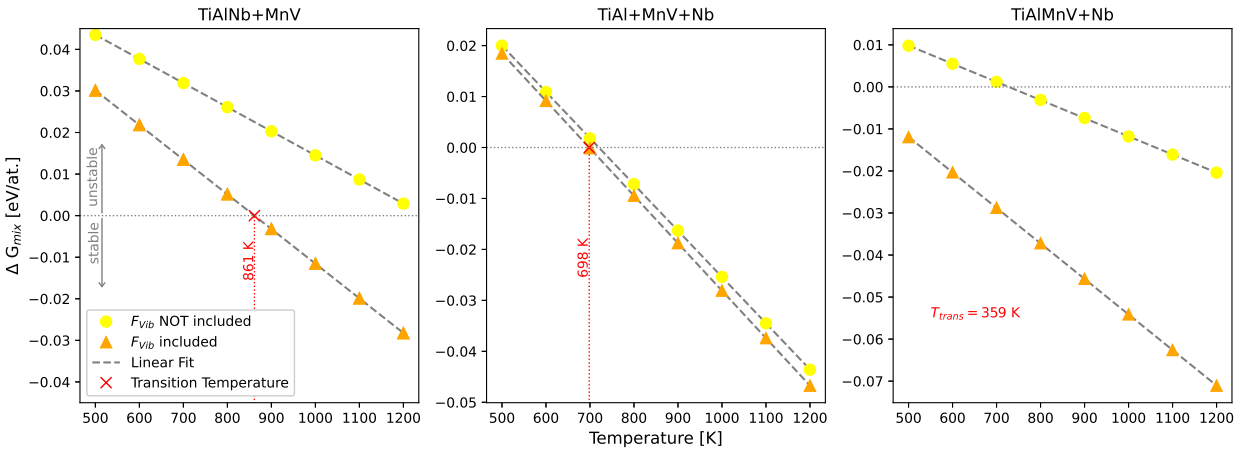

Figure 4.8: Estimated stabilization impact of the vibrational free energy on the HEAs demonstrated by the change of Gibb's free energy of the decomposition routes with the highest driving force for decomposition of TiAlNbV-Mn. The red crosses and temperatures indicate the transition temperatures from unstable to stable after including the vibrational free energy (orange values). If there is no cross as indicator, the transition temperature decreased to a value, which is out of the x-range.

Table 4.7: The transition temperatures ΔT_{trans} from a stable BCC HEA to an unstable one are summarized for the observed BCC+BCC decomposition routes. The change of T_{trans} due to the inclusion of F_{vib} is shown. The red numbers indicate the routes with highest driving force for decomposition before and after including F_{vib}.

	Decomposition Route	ΔT_{trans}
TiAlNbV-Mo	TiAlNb+MoV	877 K → 776 K
	TiAlMoNb+V	628 K → 833 K
	TiAl+MoV+Nb	483 K → 380 K
TiAlNbV-Mn	TiAlNb+MnV	1250 K → 861 K
	TiAl+MnV+Nb	720 K → 698 K
	TiAlMnV+Nb	728 K → 359 K

4.5 Experimental Observations

Colleagues from the Chair of Physical Metallurgy and Metallic Materials have performed experiments on the TiAlNbV-Mo and TiAlNbV-Mn HEAs [12]. In this section, we compare our theoretical predictions with their results. For this purpose, they provided scanning electron microscope back-scattered electron (SEM-BSE) images and data from X-ray diffraction (XRD) measurements. To gain information about the phase stability, heat treatments were applied to the HEA samples. The experimental results are presented with the kind permission of Stefan Zeisl; they were previously presented within his thesis [12].

4.5.1 Phase Stability of BCC TiAlNbV-Mo

The experimental results for TiAlNbV-Mo consisting of a BCC phase are summarised in Fig. 4.9. The SEM-BSE image (panel a)) shows the as-cast state of the HEA. In this state, the alloy consists of a single-phase solid solution with an inhomogeneous structure. The black dots indicate TiN impurities incorporated during the manufacturing process and will be neglected.

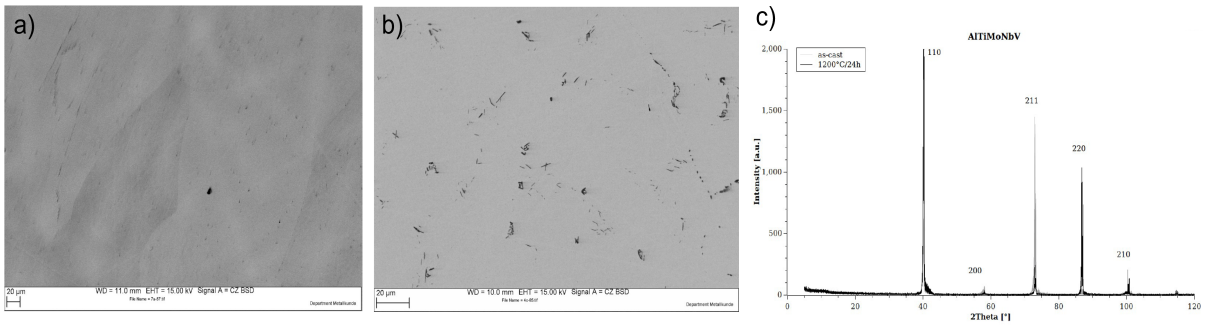

Figure 4.9: TiAlNbV-Mo HEA: a) As-cast state: Single phase solid solution with an inhomogeneous structure and TiN impurities; b) After heat treatment (1200 °C, 24 h): Single-phase solid solution with an homogeneous microstructure; c) XRD measurement after heat treatment: Single BCC phase.

After the observation of the initial state, a heat treatment at 1473 K for the duration of 24 h is executed. The resulting image is demonstrated in Fig. 4.9 b), which suggests that the microstructure has gained much more homogeneity. Hence, the assumption is that the HEA stayed in its single-phase solid solution. Additional XRD measurements (Fig. 4.9 c)) prove this assumption by detecting peaks solely for the single BCC phase, and no signs of phase transition or decomposition effects could be observed after heat treatment. From these results, it can be presumed that TiAlNbV-Mo forms a single phase BCC alloy at high temperatures and keeps it during cooling down to room temperature.

As a reminder, from the theoretical studies, we predicted that the lowest temperature below which the HEA decomposes into TiAlNb+MoV (see Fig. 4.7) is at $\approx$ 775 K. Although the practical and theoretical approaches are rather different, the outcome has only minor differences. The reason that the predicted phase stability differs at low temperatures could come from sources of errors on both sides, e.g. HEA samples used in the experiment could deviate slightly from equi- or near-equiatomic composition and also impurities can influence the evolution of the microstructure. On the other hand, in the theoretical approach, several approximations are made, e.g. only some contributions to entropy are considered or no actual kinetics of the decomposition process was taken into account. By searching for other reasons for the apparent discrepancy at low temperatures, we also consider the binary phase

diagram of MoV (Fig. 4.10). According to this phase diagram, MoV can not exist below ≈ 1100 K due to a miscibility gap. Hence, the MoV as a decomposition product is probably not predicted correctly in the theoretical model because of some approximations. This would affect the TiAlNb+MoV decomposition route, which exhibits the highest driving force for decomposition at 500 K (see 4.2). In conclusion, the investigated TiAlNbV-Mo HEA is likely a kinetically stabilized alloy, which also exhibits proper preconditions to form a single-phase BCC solid solution at lower temperatures.

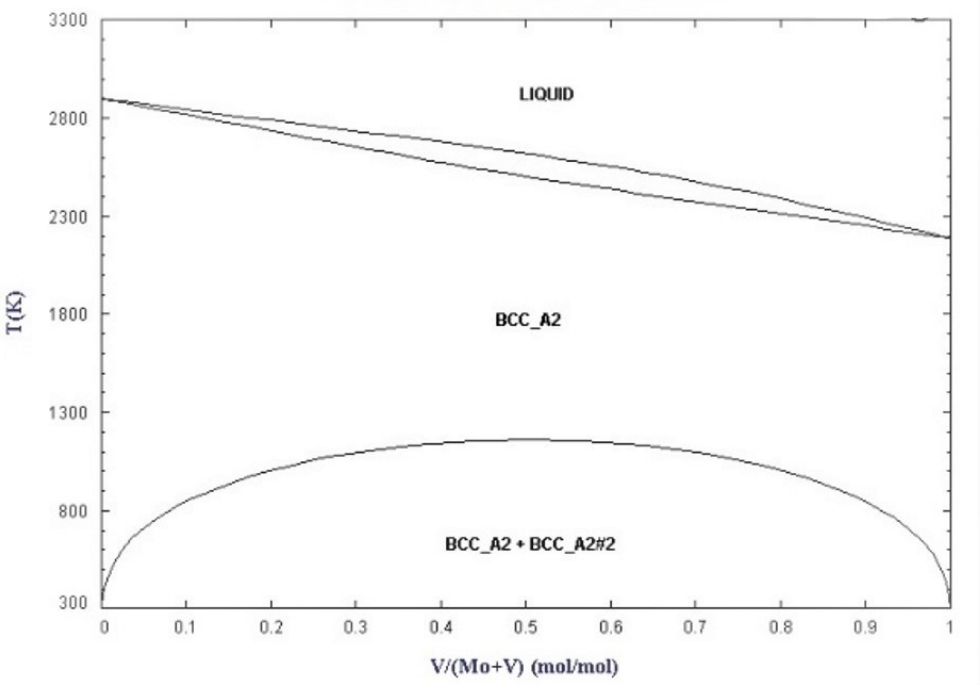

Figure 4.10: Binary phase diagram of MoV [69].

4.5.2 Phase Stability of BCC TiAlNbV-Mn

The TiAlNbV-Mn HEA was tested in the same experimental setup as the samples in the previous section. In the SEM-BSE image of the as-cast (Fig. 4.11 a)) a two-phase microstructure is observed. The exposure of the HEA to a heat treatment at ≈ 1170 K for 24 h leads to a two-phase microstructure with a significantly reduced dark phase (Fig. 4.11 b)). Zeisl [12] concluded that the dark phase corresponds to the BCC phase and the bright one the HCP phase. The XRD analysis of TiAlNbV-Mn (see Fig. 4.11 c)) confirms the assumption of a BCC(B2)+HCP(C14) microstructure. Heat treatments with different values for temperature, time or cooling rates did not yield a single-phase solid solution up to now. This is well in accordance with the computational conclusion that the TiAlNbV-Mn HEA has no tendencies to form a stable single-phase HEA, not even at high temperatures.

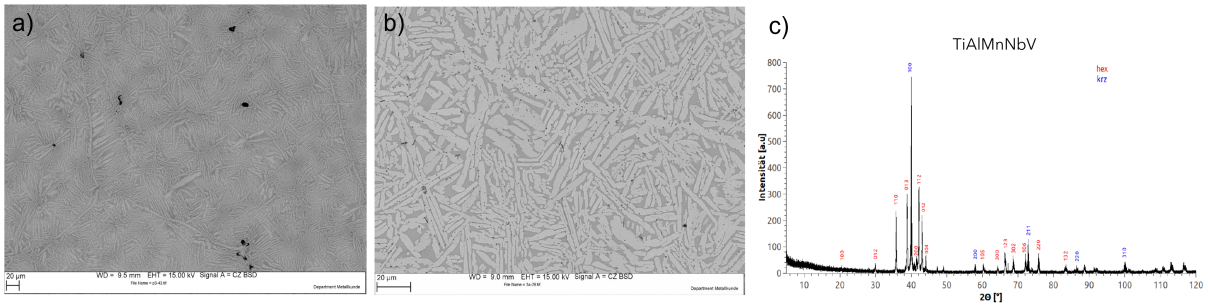

Figure 4.11: a) As Cast state: Two-phase microstructure with impurities; b) After heat treatment (900 °C, 24 h): Two-phase microstructure, where dark phase (BCC) is significantly reduced; c) XRD measurement after heat treatment: BCC(B2) + HCP(C14).

The composition of the two different phases has been measured with energy dispersive X-ray spectroscopy (EDX) after heat treatment. Based on this analysis, the HCP-C14 phase contains a much higher amount of Mn ($x_{Mn} \approx 28.6\,\%$, $x_{Ti} \approx 12.5\,\%$), the BCC phase a higher amount of Ti ($x_{Mn} \approx 11.2\,\%$, $x_{Ti} \approx 25.1\,\%$) and the other elements stay at $\approx 20\,\%$ portion. This observation gives rise to the idea that the Mn content is the critical factor for the precipitation of the HCP-C14 phase. Therefore, two other alloys have been investigated [12], in which the Mn content is increased from 20 to 30 % on the expense of Ti: $Ti_{10}Al_{20}Nb_{20}V_{20}$-$Mn_{30}$ and vice versa to $Ti_{30}Al_{20}Nb_{20}V_{20}$-$Mn_{10}$. It turns out that the microstructure of the alloy with the higher Mn ratio consists of a huge amount of HCP phase in the as-cast state. The alloy with lower Mn content solidifies in a single BCC phase structure in the as-cast state and only a little amount of HCP phase is observed after the heat treatment. Hence, the $Ti_{30}Al_{20}Nb_{20}V_{20}$-$Mn_{10}$ alloy tends to be a more promising candidate for a stable single-phase BCC solid solution. This also correlates with the conclusion of Fig.4.4, that an increasing amount of Mn stabilizes the HCP-C14 phase. Finally, it proves again that Mn is the driving force for the precipitation of the HCP-C14 phase. Probably not only the Mn content leads to decomposition, but the combination of Mn with TiAl. From a former study [15], we know that the decomposition of a TiAlMn alloy into a Laves phase (C14) has been observed as well. Therefore it can be concluded that no stable single-phase BCC HEA can be obtained by mixing Mn with a TiAl alloy due to the precipitation of the HCP-C14 phase.

4.6 Phase Stability of FCC HEAs

Literature suggests that TiAlNbV most likely solidifies in the BCC structure [10]. Moreover, the addition of Mo and Mn should stabilize the BCC phase even more because they also solidify in a BCC structure as individual elements and can be stated as BCC stabilizers [13].

On the other hand, binary TiAl is stable in a tetragonally-distorted FCC structure. Since no information about the existence or non-existence of FCC TiAlNbV-Mo or TiAlNbV-Mn is available, their phase stability has been studied as well. Ground state properties of the HEAs and also their decomposition products have been calculated with the inclusion of full structural relaxation.

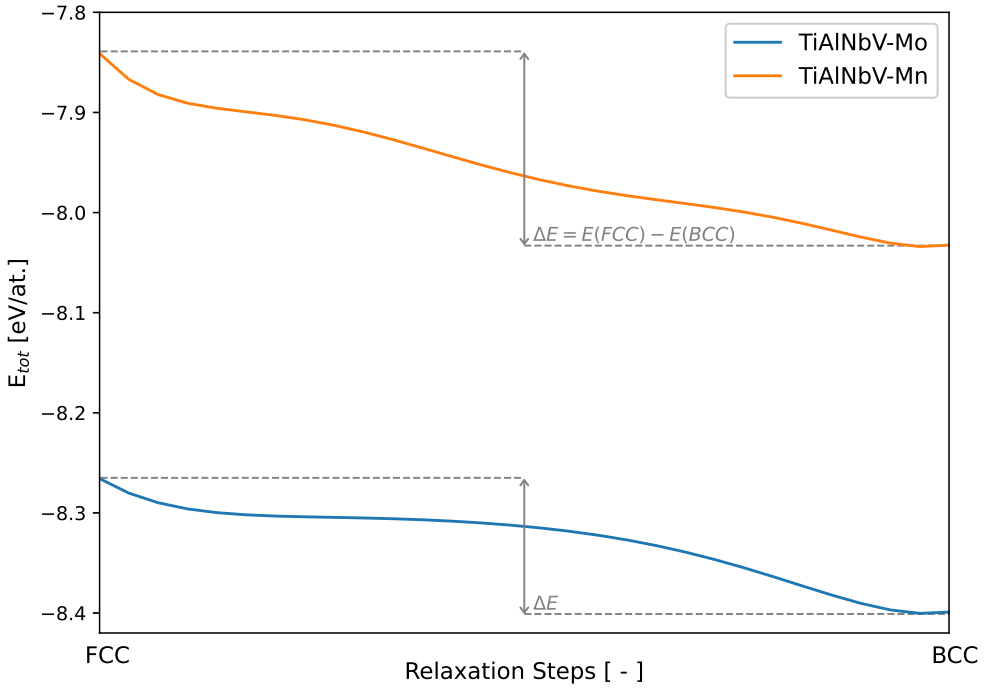

Figure 4.12: The development of the total energies during the spontaneous transformation of TiAlNbV-Mo and TiAlNbV-Mn FCC into BCC structure. ΔE denotes the difference in energy of the FCC and BCC phase.

The total energies during the relaxation are shown in Fig. 4.12 for TiAlNbV-Mo and TiAlNbV-Mn as examples. The continuous decrease of the energies implies that the structure probably transforms into a more stable one. Moreover, in the case of the HEAs, the energy difference ΔE between the initial FCC and the relaxed structure is relatively large, which often goes hand in hand with structural changes. A detailed atomic structure analysis with Ovito [70] reveals that the final structures of most systems are not FCC anymore but exhibit BCC characteristics. Screenshots of FCC TiAlNbV-Mo in its unrelaxed (Fig. 4.13) and relaxed state (Fig. 4.14) are shown as an example. The structural analysis reveals that most systems transformed from FCC to BCC structure during relaxation. The obtained structures for all FCC systems after relaxation, analyzed by Ovito, are presented in Tab. 4.8.

Moreover, the final total ground state energies of most initial FCC models are similar to the obtained energies from the calculations in Sec. 4.2, in which the initial structures are already BCC. There only exist a few exceptions that stay in FCC structure during relaxation,

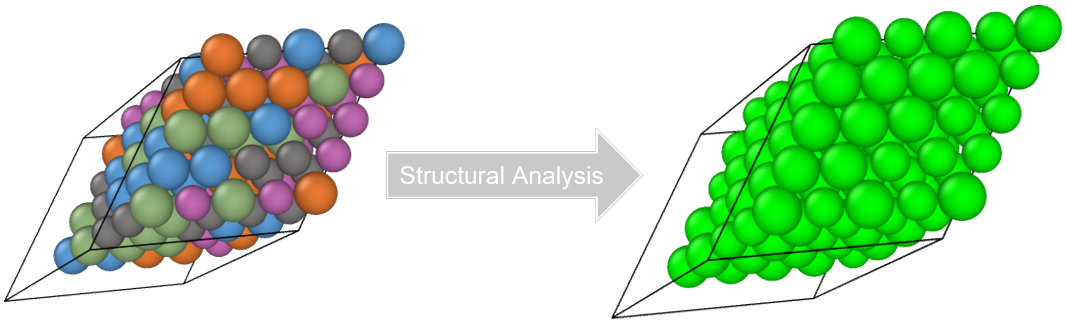

Figure 4.13: The FCC structure of the TiAlNbV-Mo HEA without and with structural analysis before any relaxation processes have been applied. The green colour denotes the identification of FCC structure.

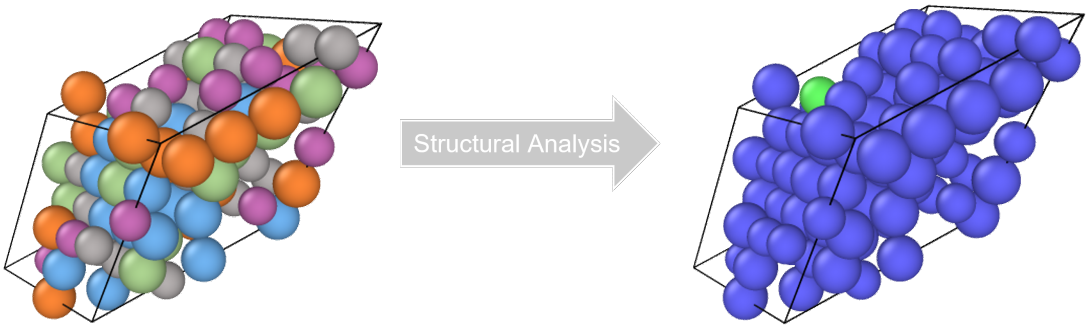

Figure 4.14: The structure of the FCC TiAlNbV-Mo HEA after relaxation without and with structural analysis. The blue colour denotes the identification of a BCC structure. A green atom, which stands for FCC structure, is still identified in the back.

namely AlNb, TiAl, AlV, TiAlNb and TiAlV. To prove the preference for the BCC structure in terms of energies, the systems, which are assumed to transform to BCC, and the systems staying in FCC are compared to the pure BCC structures from previous sections. This is done by calculating the differences of the relaxed energies between the FCC and BCC systems. The spontaneously transforming structures (Fig. 4.15 (a)) exhibit relatively low differences of total energies as demonstrated in Fig. 4.15. Mostly, the differences for these systems stay below 20 meV, which is a randomly chosen threshold for orientation purposes. The systems, which stay in FCC structure (Fig. 4.15 (b)), mostly show differences that clearly exceed 20 meV. Although exceptions on both sides are present, the convergence in the direction of the BCC ground state energies is demonstrated by the FCC $\rightarrow$ BCC results as the deviations are relatively low. The obtained higher differences of the FCC $\rightarrow$ FCC energies confirm the assumption that they stay in FCC structure. Overall, this is another proof for the spontaneous transformation from FCC into the direction of BCC and the strong

BCC preference of the HEAs, TiAlNbV-Mo and TiAlNbV-Mn. Moreover, it can be stated that the same is observed for most of the corresponding decomposition products (low-to-medium entropy alloys based on TiAl) with the initial FCC structure.

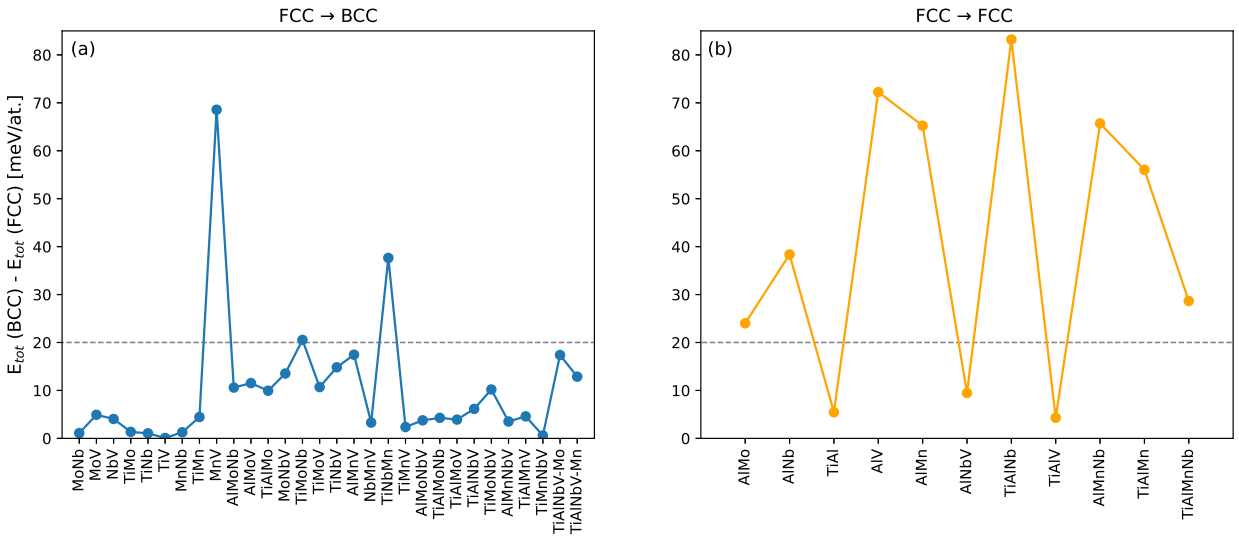

Figure 4.15: In (a), the differences of the total energies of the FCC structures (identified as BCC after relaxation) to the BCC systems are shown. In (b) the same energy difference is shown for the structures, which stayed in FCC during relaxation.

Interestingly, the stoichiometric TiAl seems to be a stabilizer of the FCC phase. This is in accordance with a study by Abdoshani *et al.* [71], in which they predicted that the TiAl system spontaneously transforms from the β-BCC to the γ-FCC phase and therefore, FCC phase is preferred. On the other hand, they claim that the addition of Mo into TiAl leads to an energetic preference for the BCC phase. This is probably the reason why all alloys containing Mo transform to BCC and only systems without Mo keep the FCC structure. It seems that also Mn features the same effect because also the TiAlMn ternary transformed from FCC to BCC structure, although no Mo is contained. This confirms that Mn acts as a BCC stabilizer. In conclusion, these results strengthen the assumption that a strong BCC preference for TiAlNbV-Mo and TiAlNbV-Mn as well as most decomposition products exists. Only alloys based on TiAl, but without the addition of Mo could form a stable FCC phase. Therefore, it is not foreseen as useful to do further research and evaluations on the phase stability of FCC TiAlNbV-Mo and TiAlNbV-Mn systems.

Table 4.8: Structures of the initial FCC systems after the relaxation process.

System	Relaxed Structure	System	Relaxed Structure
AlMo	66.6 % FCC+33.3 % BCC	TiMoNb	100 % BCC
AlNb	100 % FCC	TiMoV	100 % BCC
TiAl	100 % FCC	TiNbV	100 % BCC
AlV	100 % FCC	AlMnNb	40 % FCC+5 % BCC+55 % others
MoNb	100 % BCC	TiAlMn	37 % FCC+7 % BCC+56 % others
MoV	100 % BCC	AlMnV	100 % BCC
NbV	100 % BCC	MnNbV	100 % BCC
TiMo	100 % BCC	TiMnNb	47 % BCC+53 % others
TiNb	100 % BCC	TiMnV	100 % BCC
TiV	100 % BCC	AlMoNbV	100 % BCC
AlMn	84 % FCC+16 % others	TiAlMoNb	100 % BCC
MnNb	100 % BCC	TiAlMoV	100 % BCC
TiMn	100 % BCC	TiAlNbV	95 % BCC+5 % HCP
MnV	100 % BCC	TiMoNbV	100 % BCC
AlMoNb	100 % BCC	AlMnNbV	100 % BCC
AlMoV	100 % BCC	TiAlMnNb	5 % FCC+16 % BCC+79 % others
AlNbV	35 % FCC+55 % BCC+10 % others	TiAlMnV	100 % BCC
TiAlMo	100 % BCC	TiMnNbV	100 % BCC
TiAlNb	100 % FCC	TiAlNbV-Mo	100 % BCC
TiAlV	100 % FCC	TiAlNbV-Mn	100 % BCC
MoNbV	100 % BCC		

Chapter 5

Summary

This thesis pursued the objective of theoretically investigating the phase stability of TiAl-based HEAs, namely TiAlNbV-Mo and TiAlNbV-Mn. The goal was to find a single-phase solid solution alloy. This was done by calculating the ground-state total energies of the quinary HEAs and all their possible unary, binary, ternary and quaternary decomposition products in the BCC phase by DFT and subsequently evaluating the corresponding mixing energies. As a starting point, the mixing enthalpies of the systems were evaluated and compared with each other, which demonstrates the stability of the alloys at 0 K. Several elemental combinations yielding stable solid solutions have been identified.

Next, the entropy term has been included in the form of its configurational entropy contribution. This provided the opportunity to calculate the Gibbs free energy of mixing by additionally introducing temperature implicitly. Hence, an insight into the phase stability could be gained at different temperatures and the stabilization effect of the configurational entropy was estimated. It turned out, that the BCC TiAlNbV-Mo HEA was not fully stable.The TiAlNbV-Mn HEA exhibited a driving force for decomposition up to more than 1200 K. For this system, also the HCP-C14 phase has been considered as a decomposition product, which led to the same conclusion. The results for phase stability have been partly confirmed by comparing them with analysis by the EMTO-CPA method.

As a next step, the vibrational entropy has been involved in order to get an even more accurate description of Gibbs free energy and to estimate its additional impact on the phase stability. This has been done by implementing the elastic properties of the BCC alloys, calculated by the stress-strain method, into the harmonic Debye model. The results revealed that the HEAs mostly experience a stabilization effect by introducing the vibrational entropy term. It shifts the transition temperature, which denotes the crossover from positive to negative Gibbs free energy of mixing, to lower values. Nonetheless, the effect is not significant enough, and neither TiAlNbV-Mo nor TiAlNbV-Mn represented stable BCC HEAs down to low temperatures even with this further stabilization. Moreover, it has been shown that

the consideration of vibrational entropy could also lead to a destabilization of the HEAs for certain decomposition routes.

The comparison with experimental methods gave insight into the microstructural evolution of the BCC HEAs. The TiAlNbV-Mo HEA has been observed to be stable down to room temperature after heat treatment. Hence, no decomposition effects are discovered, which does not fully agree with the theoretical conclusion. Therefore, TiAlNbV-Mo is proposed to be most likely a kinetically stabilized HEA and has good prerequisites for further alloy development. The outcome for BCC TiAlNbV-Mn is in accordance with the theoretical results as a two-phase BCC+HCP microstructure has been detected also in experiments.

Finally, also the phase stability of FCC TiAlNbV-Mo and TiAlNbV-Mn was investigated. However, a spontaneous transformation of the FCC HEAs to BCC occurred during the relaxation processes proving the genuine instability of the FCC structures. Hence, any additional study of phase stability would have been misleading. Nevertheless, this has been the confirmation that a strong preference for the BCC phase exists for the studied HEAs.

Bibliography

[1] F. Liu, P. K. Liaw, and Y. Zhang, Metals **12**, 501 (2022).

[2] M.-H. Tsai and J.-W. Yeh, Materials Research Letters **2**, 107 (2014).

[3] I. Florea, R. Florea, O. Bălţătescu, V. Soare, R. Chelariu, I. Carcea, *et al.*, Journal of Optoelectronics and Advanced Materials **15**, 761 (2013).

[4] B. Cantor, I. Chang, P. Knight, and A. Vincent, Materials Science and Engineering: A **375-377**, 213 (2004).

[5] W. Kohn and L. J. Sham, Physical review **140**, A1133 (1965).

[6] G. Kresse and D. Joubert, Phys. Rev. B Condens. Matter **59**, 1758 (1999).

[7] G. Kresse, M. Marsman, and J. Furthmüller, "VASP The GUIDE," (2015).

[8] J. Chen, X. Zhou, W. Wang, B. Liu, Y. Lv, W. Yang, D. Xu, and Y. Liu, Journal of Alloys and Compounds **760**, 15 (2018).

[9] D. Batalu, G. Cosmeleata, and A. Aloman, UPB Sci. Bull. Ser. B Chem. Mater. Sci **68**, 77 (2006).

[10] N. Stepanov, D. Shaysultanov, G. Salishchev, and M. Tikhonovsky, Materials Letters **142**, 153 (2015).

[11] B. Schuh, B. Völker, V. Maier-Kiener, J. Todt, J. Li, and A. Hohenwarter, Advanced Engineering Materials **19**, 1600674 (2017).

[12] S. Zeisl, "Development of a high entropy alloy for high temperature applications," (2020), unpublished master thesis.

[13] S. Mayer, P. Erdely, F. D. Fischer, D. Holec, M. Kastenhuber, T. Klein, and H. Clemens, Advanced Engineering Materials **19**, 1600735 (2017).

[14] A. Lacour-Gogny-Goubert, Z. Zhao-Huvelin, A. Bachelier-Locq, I. Guillot, and A. Denquin, in *Materials Science Forum*, Vol. 941 (Trans Tech Publ, 2018) pp. 1111–1116.

[15] M. Jop, *Development and characterization of new low-cost intermetallic titanium aluminide alloys for advanced environmental-friendly propulsion systems*, Master's thesis, University of Leoben (2020).

[16] J. Daintith, *A dictionary of chemistry* (OUP Oxford, 2008).

[17] Y. Zhang, T. T. Zuo, Z. Tang, M. C. Gao, K. A. Dahmen, P. K. Liaw, and Z. P. Lu, Progress in materials science **61**, 1 (2014).

[18] F. D. C. Garcia Filho, R. O. Ritchie, M. A. Meyers, and S. N. Monteiro, Journal of Materials Research and Technology **17**, 1868 (2022).

[19] S. Gorsse, D. B. Miracle, and O. N. Senkov, Acta Materialia **135**, 177 (2017).

[20] S. Gorsse, J.-P. Couzinié, and D. B. Miracle, Comptes Rendus Physique **19**, 721 (2018).

[21] M.-H. Tsai, Entropy **15**, 5338 (2013).

[22] B. Cantor, Progress in Materials Science **120**, 100754 (2021).

[23] H.-W. Luan, Y. Shao, J.-F. Li, W.-L. Mao, Z.-D. Han, C. Shao, and K.-F. Yao, Scripta Materialia **179**, 40 (2020).

[24] Y. Jien-Wei, Ann. Chim. Sci. Mat **31**, 633 (2006).

[25] K.-H. Cheng, C.-H. Lai, S.-J. Lin, and J.-W. Yeh, in *Annales de chimie (Paris. 1914)*, Vol. 31 (2006) pp. 723–736.

[26] J. Dabrowa, M. Zajusz, W. Kucza, G. Cieślak, K. Berent, T. Czeppe, T. Kulik, and M. Danielewski, Journal of Alloys and Compounds **783**, 193 (2019).

[27] C. G. Schön, M. A. Tunes, R. Arróyave, and J. Ågren, Calphad **68**, 101713 (2020).

[28] C.-C. Yen, G.-R. Huang, Y.-C. Tan, H.-W. Yeh, D.-J. Luo, K.-T. Hsieh, E.-W. Huang, J.-W. Yeh, S.-J. Lin, C.-C. Wang, *et al.*, Journal of Alloys and Compounds **818**, 152876 (2020).

[29] C. Lee, G. Song, M. C. Gao, R. Feng, P. Chen, J. Brechtl, Y. Chen, K. An, W. Guo, J. D. Poplawsky, *et al.*, Acta Materialia **160**, 158 (2018).

[30] W. Hume-Rothery, *Researches on the nature, properties, and conditions of formation of intermetallic compounds, with special reference to certain compounds of tin*, Ph.D. thesis, University of London (1926).

[31] Q. He, Y. Ye, and Y. Yang, Journal of Phase Equilibria and Diffusion **38**, 416 (2017).

[32] M. C. Troparevsky, J. R. Morris, M. Daene, Y. Wang, A. R. Lupini, and G. M. Stocks, Jom **67**, 2350 (2015).

[33] N. Stepanov, N. Y. Yurchenko, D. Skibin, M. Tikhonovsky, and G. Salishchev, Journal of Alloys and Compounds **652**, 266 (2015).

[34] N. Y. Yurchenko, N. Stepanov, S. Zherebtsov, M. Tikhonovsky, and G. Salishchev, Materials Science and Engineering: A **704**, 82 (2017).

[35] "The Merck Periodic Table of Elements," https://www.merckgroup.com/en/company/periodic-table-of-elements-app.html, accessed: 2022-08-08.

[36] A. Kretschmer, D. Holec, K. Yalamanchili, H. Rudigier, M. Hans, J. M. Schneider, and P. H. Mayrhofer, Acta Materialia **224**, 117483 (2022).

[37] C. Höglund, B. Alling, J. Birch, M. Beckers, P. O. Å. Persson, C. Baehtz, Z. Czigány, J. Jensen, and L. Hultman, Phys. Rev. B Condens. Matter **81**, 224101 (2010).

[38] P. H. Mayrhofer, F. D. Fischer, H. J. Böhm, C. Mitterer, and J. M. Schneider, Acta Materialia **55**, 1441 (2007).

[39] C. Kittel and P. McEuen, *Introduction to solid state physics* (John Wiley & Sons, 2018).

[40] A. Breidi, "Quasiharmonic debye model," (2016).

[41] T. Chakraborty, J. Rogal, and R. Drautz, Physical Review B **94**, 224104 (2016).

[42] R. Yu, J. Zhu, and H. Ye, Computer physics communications **181**, 671 (2010).

[43] A. Saengdeejing, Y. Chen, K. Suzuki, H. Miura, and T. Mohri, Computational materials science **70**, 100 (2013).

[44] M. Moakher and A. N. Norris, Journal of Elasticity **85**, 215 (2006).

[45] W. Voigt, BG Teubner, Leipzig und Berlin (1928).

[46] A. Reuß, ZAMM-Journal of Applied Mathematics and Mechanics/Zeitschrift für Angewandte Mathematik und Mechanik **9**, 49 (1929).

[47] R. Hill, Proceedings of the Physical Society. Section A **65**, 349 (1952).

[48] L. d. Broglie, The London, Edinburgh, and Dublin Philosophical Magazine and Journal of Science **47**, 446 (1924).

[49] E. Schrödinger, Physical review **28**, 1049 (1926).

[50] J. G. Lee, *Computational materials science: an introduction* (CRC Press, 2016).

[51] R. E. Hummel, *Electronic properties of materials* (Springer Science & Business Media, 2011) pp. 15–75.

[52] D. R. Hartree, in *Mathematical Proceedings of the Cambridge Philosophical Society*, Vol. 24 (Cambridge university press, 1928) pp. 89–110.

[53] M. Born and R. Oppenheimer, Annals of Physics **84**, 547 (1927).

[54] K. Burke, "The ABC of DFT," https://dft.uci.edu/doc/g1.pdf (2007).

[55] P. Hohenberg and W. Kohn, Physical review **136**, B864 (1964).

[56] J. P. Perdew, K. Burke, and M. Ernzerhof, Phys. Rev. Lett. **77**, 3865 (1996).

[57] G. Kresse and D. Joubert, Physical review b **59**, 1758 (1999).

[58] A. W. Leissa, Journal of Sound and Vibration **287**, 961 (2005).

[59] J. D. Pack and H. J. Monkhorst, Physical Review B **16**, 1748 (1977).

[60] A. Zunger, S.-H. Wei, L. Ferreira, and J. E. Bernard, Physical review letters **65**, 353 (1990).

[61] A. Van De Walle, Calphad **33**, 266 (2009).

[62] "The VASP Manual," https://www.vasp.at/wiki/index.php/The_VASP_Manual, accessed: 2022-07-26.

[63] L. Vitos, *Computational quantum mechanics for materials engineers: the EMTO method and applications* (Springer Science & Business Media, 2007).

[64] D. Gehringer, "sqsgenerator Documentation," https://sqsgenerator.readthedocs.io/en/latest/, accessed: 2022-07-29.

[65] M. Born and K. Huang, London, New York (1954).

[66] A. Jain, S. P. Ong, G. Hautier, W. Chen, W. D. Richards, S. Dacek, S. Cholia, D. Gunter, D. Skinner, G. Ceder, and K. a. Persson, APL Materials **1**, 011002 (2013).

[67] K. Persson, "Materials data on nb (sg:225) by materials project," (2016).

[68] K. Persson, "Materials data on v (sg:229) by materials project," (2014).

[69] J. Bratberg, *CALPHAD*, Vol. 26 (2002) pp. 459–476, accessed online via FactSage alloy database.

[70] A. Stukowski, Modelling and simulation in materials science and engineering **18**, 015012 (2009).

[71] N. Abdoshahi, P. Spoerk-Erdely, M. Friák, S. Mayer, M. Šob, and D. Holec, Physical Review Materials **4**, 103604 (2020).

Appendix A

Estimation of Maximum Strain for Stress-Strain Method

For the application of the stress-strain method (see Sec. 2.7), it is important to stay in the elastic regime. To obtain the information on the maximum strain that can be applied, the method is performed for several magnitudes of maximum strain ε_{max} on the example of Mo BCC. From Fig. A.1 it can be seen that the trend lines are in an acceptable range of deviation until $\varepsilon_{max} \approx 0.3$. Especially in the graphs of C_{11} and C_{12}, a distinct increase or decrease of the values is observed, which leads to the conclusion that the elastic regime is left.

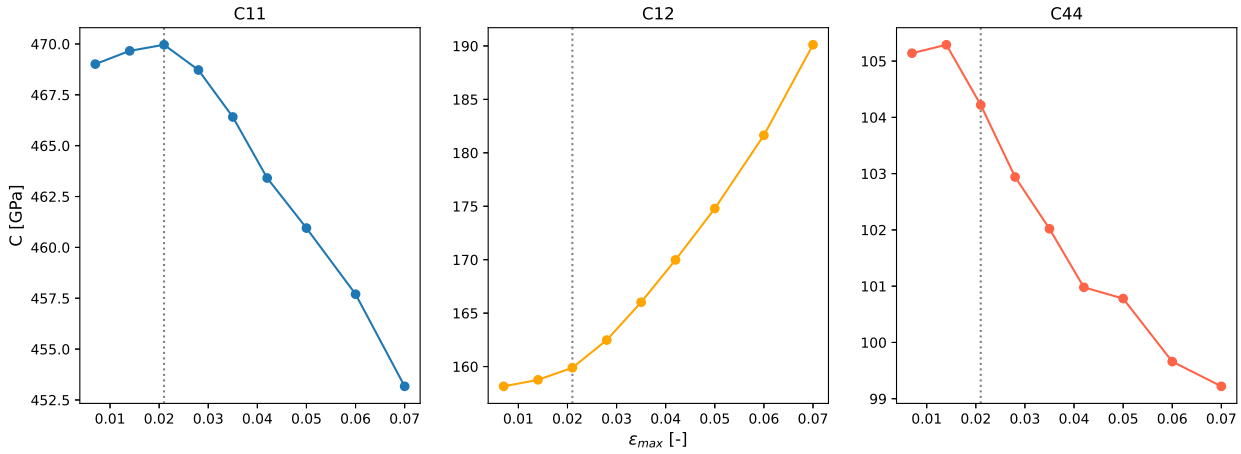

Figure A.1: The three cubic elastic constants for Mo BCC at different maximum strains ε_{max} obtained by the stress-strain method. The grey line indicates $\varepsilon_{max} = 0.021$, which is used for the elasticity calculations in this thesis.

The bulk modulus is represented separately in Fig. A.2 at different ε_{max}. Also from here an $\varepsilon_{max} = 0.03$ can be determined as a threshold value for the elastic regime. To have full certainty for accurate results, the optimum value for ε_{max} is determined as $\varepsilon_{max} = 0.021$.

This value is chosen for the calculation of elastic constants with the stress-strain method for all alloy systems.

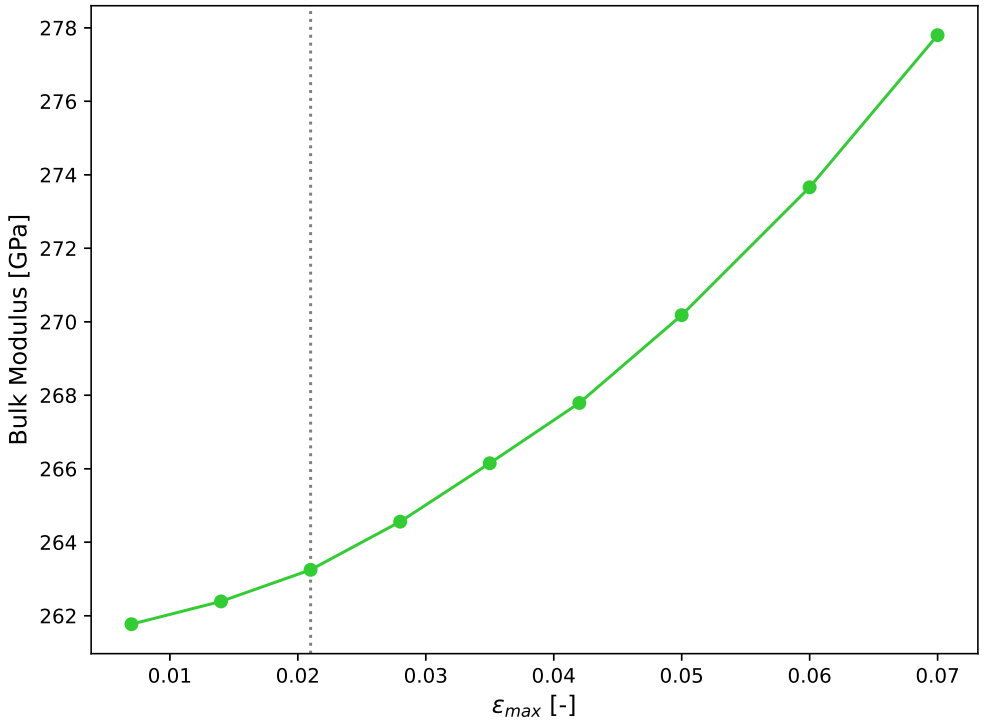

Figure A.2: The bulk modulus for Mo BCC at different maximum strains ε_{max} obtained by the stress-strain method. The grey line indicates $\varepsilon_{max} = 0.021$, which is used elasticity calculations in this thesis.

Appendix B

Further Analysis on Configurational Entropy

The configurational entropies S_{conf} for products of three different decomposition routes, TiAlMnV+Nb, TiMnV+AlNb and TiAl+MnV+Nb, as well as for the corresponding HEA are calculated and shown in Table B.1. The unary elements exhibit a S_{conf} of zero, and hence Nb is not mentioned in the table.

Table B.1: Configurational entropies S_{conf} of selected systems calculated by Eq. 2.5.

System	S_{conf} [meV/K]
AlNb	0.0200
TiAl	0.0200
MnV	0.0259
TiMnV	0.0411
TiAlMnV	0.0507
TiAlNbV-Mn	0.0575

The entropies increase, as expected, with increasing number of elements in the alloy. The different impact of temperature T on the Gibbs free energy of mixing ΔG_{mix} for decomposition routes with a different number of products is demonstrated by the equations below (Eq. B.1, Eq. B.2, Eq. B.3). The statement is, that decomposition routes with a higher number of products affect ΔG_{mix} to a larger extent due to its higher ΔS_{conf} with respect to the HEA. This is confirmed with the following equations, which demonstrates the $T\Delta S_{conf}$ term extracted from Eq. 2.6.

TiAlMnV+Nb:

$$
\begin{aligned}
&T \times \{S_{\text{conf}}(\text{TiAlNbVMn}) - [x(\text{TiAlMnV})S_{\text{conf}}(\text{TiAlMnV}) + x(\text{Nb})S_{\text{conf}}(\text{Nb})]\} = \\
&= T \times 0.0575 \ \frac{\text{meV}}{\text{K}} - [0.8 \times 0.0507 \ \frac{\text{meV}}{\text{K}} + 0.2 \times 0 \ \frac{\text{meV}}{\text{K}}]\} = \\
&= T \times \mathbf{0.0169} \ \frac{\mathbf{meV}}{\mathbf{K}}
\end{aligned}
\tag{B.1}
$$

TiMnV+AlNb:

$$
\begin{aligned}
&T \times \{S_{\text{conf}}(\text{TiAlNbVMn}) - [x(\text{TiMnV})S_{\text{conf}}(\text{TiMnV}) + x(\text{AlNb})S_{\text{conf}}(\text{AlNb})]\} = \\
&= T \times \{0.0575 \ \frac{\text{meV}}{\text{K}} - [0.6 \times 0.0411 \ \frac{\text{meV}}{\text{K}} + 0.4 \times 0.0200 \ \frac{\text{meV}}{\text{K}}]\} = \\
&= T \times \mathbf{0.0248} \ \frac{\mathbf{meV}}{\mathbf{K}}
\end{aligned}
\tag{B.2}
$$

TiAl+MnV+Nb:

$$
\begin{aligned}
&T \times \{S_{\text{conf}}(\text{TiAlNbVMn}) - \\
&- [x(\text{TiAl})S_{\text{conf}}(\text{TiAl}) + x(\text{MnV})S_{\text{conf}}(\text{MnV}) + x(\text{Nb})S_{\text{conf}}(\text{Nb})]\} = \\
&= T \times \{0.0575 \ \frac{\text{meV}}{\text{K}} - \\
&- [0.4 \times 0.0411 \ \frac{\text{meV}}{\text{K}} + 0.4 \times 0.0200 \ \frac{\text{meV}}{\text{K}} + 0.2 \times 0 \ \frac{\text{meV}}{\text{K}}]\} = \\
&= T \times \mathbf{0.0391} \ \frac{\mathbf{meV}}{\mathbf{K}}
\end{aligned}
\tag{B.3}
$$

These equations clearly confirm the statement above as the TiAl+MnV+Nb route (with highest number of decomposition products) exhibits the highest value of ΔS_{conf} with respect to the HEA. Hence, temperature has a more pronounced effect on ΔG_{mix}.